

Hyperbolic Graph Neural Networks Under the Microscope: The Role of Geometry–Task Alignment

Dionisia Naddeo ^{*1} Jonas Linkerhägner ^{*2} Nicola Toschi ^{1,3} Geri Skenderi ⁴ Veronica Lachi ⁵

Abstract

Many complex networks exhibit hyperbolic structural properties, making hyperbolic space a natural candidate for representing hierarchical and tree-like graphs with low distortion. Based on this observation, Hyperbolic Graph Neural Networks (HGNNS) have been widely adopted as a principled choice for representation learning on tree-like graphs. In this work, we question this paradigm by proposing an additional condition of geometry–task alignment, i.e., whether the metric structure of the target follows that of the input graph. We theoretically and empirically demonstrate the capability of HGNNS to recover low-distortion representations on two synthetic regression problems, and show that their geometric inductive bias becomes helpful when the problem requires preserving metric structure. Additionally, we evaluate HGNNS on the tasks of link prediction and node classification by jointly analyzing predictive performance and embedding distortion, revealing that only link prediction is geometry-aligned. Overall, our findings shift the focus from only asking *Is the graph hyperbolic?* to also questioning *Is the task aligned with hyperbolic geometry?*, showing that HGNNS consistently outperform Euclidean models under such alignment, while their advantage vanishes otherwise.

1. Introduction

Graph representation learning has gathered increasing attention over the last decade, due to the importance of solving downstream tasks such as node classification or link

^{*}Equal contribution ¹Department of Biomedicine and Prevention, University of Tor Vergata, Rome, Italy ²Department of Mathematics and Computer Science, University of Basel, Switzerland

³A.A. Martinos Center for Biomedical Imaging, Harvard Medical School, Boston, USA ⁴Bocconi Institute for Data Science and Analytics, Bocconi University, Milan, Italy ⁵Department of Physics and Technology, UiT The Arctic University of Norway, Tromsø, Norway. Correspondence to: V.L. <veronica.lachi@uit.no>.

Preprint. February 3, 2026.

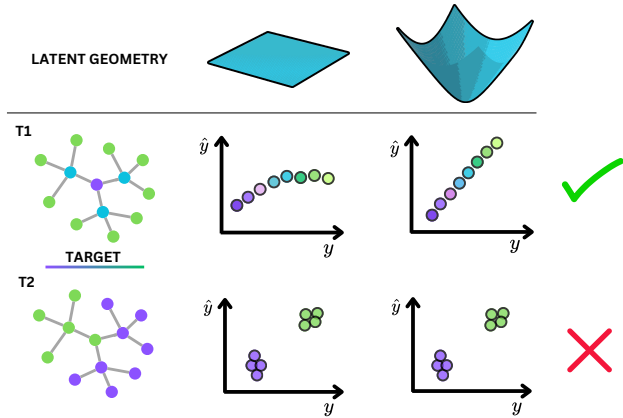


Figure 1. Geometry–Task Alignment. Different latent geometries induce different degrees of alignment between embeddings and the prediction task. The top row depicts a latent manifold with increasing curvature magnitude, while the bottom rows plot the predictions \hat{y} against the targets y . The first task (**T1**) benefits from the non-flat latent geometry since the targets require such a geometric inductive bias. On the other hand, no benefits can be observed when solving **T2** despite the input graph being the same. For graphs with hyperbolic structure, decreasing latent curvature can make a task that is poorly represented in flat space become progressively more solvable, provided that the targets are aligned with the underlying input data geometry.

prediction (Khosraftar & An, 2024). Early embedding approaches such as DEEPWALK (Perozzi et al., 2014) and NODE2VEC (Grover & Leskovec, 2016) focused on learning low-dimensional node representations in Euclidean space by relying on random-walk co-occurrence statistics, producing representations intended to reflect graph proximity. The core premise behind the embedding paradigm is, therefore, *geometric faithfulness*: a good graph embedding should preserve the relevant structure of the input graph.

This naturally raises the question of which geometry is appropriate to maintain this faithfulness. Many real-world networks exhibit strong hierarchical organization and tree-like growth patterns, including biological taxonomies (Matsumoto et al., 2021), knowledge graphs (Kolovakis et al., 2020), and social hierarchies (Yang et al., 2023). From a metric viewpoint, tree-like graphs are closely connected

to negatively curved spaces. Crucially, Sarkar (2011) provided a guarantee: for a fixed low dimensionality, trees can be embedded in hyperbolic space with arbitrarily small distortion, while this cannot be done in Euclidean space. Motivated by this theory, hyperbolic representation learning has emerged as a powerful tool to encode latent hierarchies (Nickel & Kiela, 2018; Kitsak et al., 2020; Wang et al., 2019; Chami et al., 2020; Pan & Wang, 2021). In particular, Nickel & Kiela (2017) introduced Poincaré embeddings, demonstrating that hyperbolic geometry yields low-distortion representations of hierarchical symbolic data and relational structures.

The landscape of graph learning changed with the advent of Graph Neural Networks (GNNs) (Scarselli et al., 2008; Kipf & Welling, 2017; Hamilton et al., 2017; Veličković et al., 2018). Rather than explicitly learning embeddings, GNNs learn node representations through a message passing procedure in such a way that a specified task loss is minimized. Inspired by the success of hyperbolic embeddings, several works proposed Hyperbolic GNNs (HGNNs) to perform message passing in hyperbolic spaces (Liu et al., 2019; Chami et al., 2019; Zhang et al., 2021; Chen et al., 2022). This line of work has fostered the belief that *HGNNs should be preferred whenever the input graph is highly hyperbolic*, which is often measured using Gromov’s (1987) δ -hyperbolicity.

Despite their popularity in several applications like brain network analysis, recommender systems, and knowledge graphs (Baker et al., 2024; Yang et al., 2023; Li et al., 2024), the benefits of HGNNs remain contested. Recent work suggests that the empirical advantages of HGNNs are difficult to assess on standard benchmarks, where tasks can often be solved from node features alone (Katsman & Gilbert, 2025). Naddeo et al. (2024) further show that, on graph-level tasks, HGNNs often fail to consistently outperform Euclidean models, even on strongly hyperbolic graphs. These findings highlight an important, yet underexplored, conceptual gap in the current narrative. The original motivation for hyperbolic *embeddings* was fundamentally to have minimal distortion. In contrast, supervised GNN representations are task-driven and therefore do not necessarily optimize for metric faithfulness. Consequently, even if hyperbolic space is the right geometry for *the input*, it does not follow that hyperbolic message passing is beneficial for *the task at hand*. Specifically, while trees admit near-isometric hyperbolic embeddings (Sarkar, 2011), it has never been established that hyperbolic message passing under supervision actually recovers low-distortion node geometries, nor that such low distortion is systematically useful across different graph learning tasks.

In this work, we revisit the question of when HGNNs are truly warranted through the lens of *geometric alignment*

between input structure and task supervision (Fig. 1). We argue that the “tree-likeness” of the input graph is not, by itself, a sufficient criterion, but we must consider an additional aspect, i.e., whether solving the downstream task requires to reflect (parts of) the hyperbolic input geometry. Through controlled experiments on synthetic graphs, evaluations on real-world datasets, and theoretical analyses, we disentangle the benefits of learning hyperbolic representations in GNNs and when they translate into measurable performance gains. For full reproducibility, we provide our code [here](#). In summary, our main contributions are:

- (i) We empirically verify that HGNNs can recover low-distortion representations much better than their Euclidean counterparts when needed. Motivated by established theoretical results, we verify that this gap can be reduced as hidden dimensionality increases;
- (ii) We demonstrate, both through theoretical analyses and experiments, that the performance advantage of HGNNs is governed not only by the hyperbolicity of the input graph but also by the alignment of the supervision signal with the metric structure of the input;
- (iii) We derive actionable guidance for practitioners: hyperbolic GNNs are well suited for link prediction on tree-like graphs due to task–geometry alignment, are generally unnecessary for node classification where separability dominates, and may benefit node regression, although the lack of appropriate benchmarks remains an open research gap.

2. Background

In this section, we briefly introduce the key concepts from hyperbolic geometry used in this paper and review the main types of hyperbolic graph learning methods. Further details on related works and hyperbolic geometry appear in Appendices A and B.

Riemannian Manifolds and Hyperbolic Space A Riemannian manifold (\mathcal{M}, g) is a smooth manifold equipped with a metric $g_x : T_x \mathcal{M} \times T_x \mathcal{M} \rightarrow \mathbb{R}$ at each point $x \in \mathcal{M}$, where $T_x \mathcal{M}$ denotes the tangent space at x . The metric g defines a (local) inner product thereby leading to notions of length and curvature, enabling the extension of Euclidean geometry to non-flat spaces. Hyperbolic space is a Riemannian manifold with constant negative sectional curvature, which induces exponential volume growth (see Appendix B.1) and makes it suitable for modeling tree-like data, where the number of nodes grows exponentially with depth. Common representations of hyperbolic space include the Poincaré ball and the Lorentz hyperboloid, which are isometric.

Poincaré ball model. The Poincaré ball \mathcal{B}_c^d represents hyperbolic space as an open ball inside \mathbb{R}^d :

$$\mathcal{B}_c^d = \left\{ \mathbf{x} \in \mathbb{R}^d : \|\mathbf{x}\|^2 < \frac{1}{c} \right\}, \quad (1)$$

equipped with a conformal metric with factor $\lambda_c(\mathbf{x}) = \frac{2}{1-c\|\mathbf{x}\|^2}$, where $c > 0$ is the magnitude of the curvature. The metric is in fact an appropriately scaled version of the Euclidean one. Points lie inside a bounded Euclidean region, yet the hyperbolic distance increases infinitely near the boundary. This yields a useful geometric picture: points closer to the boundary are far away in hyperbolic distance, reflecting the behavior of leaf nodes in a hierarchy far apart, while ancestor nodes can be thought as being closer to the origin (Nickel & Kiela, 2017).

Lorentz hyperboloid model. The Lorentz model \mathcal{L}_c^d represents hyperbolic space as the d -dimensional sheet of a two-sheeted hyperboloid embedded in \mathbb{R}^{d+1} :

$$\mathcal{L}_c^d = \left\{ \mathbf{x} \in \mathbb{R}^{d+1} : \langle \mathbf{x}, \mathbf{x} \rangle_{\mathcal{L}} = -\frac{1}{c}, x_0 > 0 \right\}, \quad (2)$$

where $\langle \cdot, \cdot \rangle_{\mathcal{L}}$ is the Lorentzian inner product $\langle \mathbf{x}, \mathbf{y} \rangle_{\mathcal{L}} = -x_0 y_0 + \sum_{i=1}^d x_i y_i$. The metric of this space is in fact the induced from its ambient space, i.e., we restrict the Lorentzian inner product to the tangent spaces of the d -dimensional hyperboloid sheet.

Geodesics, exponential map, and logarithmic map. In curved spaces, the notion of straight line is replaced by *geodesics*, i.e., locally shortest curves under the manifold metric. The *exponential map* $\exp_{\mathbf{x}} : T_{\mathbf{x}}\mathcal{M} \rightarrow \mathcal{M}$ maps a tangent vector to the manifold by following the geodesic starting at \mathbf{x} with that initial velocity. Conversely, the *logarithmic map* $\log_{\mathbf{x}} : \mathcal{M} \rightarrow T_{\mathbf{x}}\mathcal{M}$ locally inverts the above map and sends a point on the manifold back to a tangent vector. These operations enable neural architectures to apply Euclidean computations by mapping back and forth into the manifold (Ganea et al., 2018; Chami et al., 2019).

2.1. HGNNS

HGNNS learn node representations in a negatively curved space and require aggregation and update operators that are consistent with hyperbolic geometry. Existing approaches can be grouped into two design families. *Tangent-space HGNNS*, such as HGCN (Chami et al., 2019), perform message passing in a Euclidean tangent space (typically at the origin) and then map the updated features back to the manifold via logarithmic and exponential maps. In contrast, *fully hyperbolic GNNs*, such as HyboNet (Chen et al., 2022), operate directly in hyperbolic space by aggregating neighborhoods with geometry-aware operators. Additional details

are provided in Appendix B.2. In our experiments, we use HGCN in the Poincaré ball model with learnable curvature, HyboNet in the Lorentz model, and GCN (Kipf & Welling, 2017) and GAT (Veličković et al., 2018) as Euclidean baselines. Note that HyboNet is designed to work only on the Lorentz hyperboloid.

3. Can HGNNs learn low-distortion embeddings of trees?

HGNNS learn representations through supervised message passing rather than by directly optimizing a metric embedding objective. This raises a basic question: *can a HGNN actually learn low-distortion representations under supervision?* To answer it, we first formally define distortion, and then relate it to a controlled synthetic task which we can learn to solve, thereby directly answering the question. It will be useful for our subsequent analyses to view a GNN as a composition of functions $f_{\theta} = g_{\psi} \circ h_{\phi}$, where h_{ϕ} is an *embedding* function and g_{ψ} is a task-dependent *solver*. Concretely, $h_{\phi} : \mathcal{G} \rightarrow \mathcal{M} \subseteq \mathbb{R}^d$ maps nodes (and their graph context) into a (Riemannian) representation manifold \mathcal{M} , while the solver $g_{\psi} : \mathcal{M} \rightarrow \mathcal{Y}$ maps latent representations to an output space \mathcal{Y} determined by the task. For example, $\mathcal{Y} = \mathbb{R}$ in node regression or $\mathcal{Y} = \{1, \dots, C\}$ in node classification. Note that whenever we refer to the maps h_{ϕ} and g_{ψ} in the context of geometric analyses below we will drop the weight subscript for simplicity.

The central object capturing the metric faithfulness of learned representations is the distortion of the embedding map h . To define this object, we first need to consider the embedding as a map between metric spaces, thus we endow the input graph $\mathcal{G} = (\mathcal{V}, \mathcal{E})$ with the shortest-path metric $d_{\mathcal{G}}(\cdot, \cdot)$ and we denote by $d_{\mathcal{M}}(\cdot, \cdot)$ the geodesic distance on the manifold \mathcal{M} .

Definition 3.1 (Embedding distortion (Sarkar, 2011)). Let $h : (\mathcal{G}, d_{\mathcal{G}}) \rightarrow (\mathcal{M}, d_{\mathcal{M}})$ be an injective map between metric spaces. Define the contraction and expansion factors:

$$\delta_c(h) = \max_{\substack{i, j \in \mathcal{V} \\ i \neq j}} \frac{d_{\mathcal{G}}(i, j)}{d_{\mathcal{M}}(h(\mathbf{x}_i), h(\mathbf{x}_j))} \quad \text{and} \quad (3)$$

$$\delta_e(h) = \max_{\substack{i, j \in \mathcal{V} \\ i \neq j}} \frac{d_{\mathcal{M}}(h(\mathbf{x}_i), h(\mathbf{x}_j))}{d_{\mathcal{G}}(i, j)}. \quad (4)$$

The distortion of h is $\delta(h) = \delta_c(h)\delta_e(h)$.

It is immediate to see that $\delta(h) \geq 1$. Moreover, from the two expressions above we have that for all $i \neq j$:

$$\frac{1}{\delta_c(h)} d_{\mathcal{G}}(i, j) \leq d_{\mathcal{M}}(h(\mathbf{x}_i), h(\mathbf{x}_j)) \leq \delta_e(h) d_{\mathcal{G}}(i, j), \quad (5)$$

so h is bi-Lipschitz onto its image with constants decided by the distortion. In particular, when $\delta(h) = 1$ we can

write $\delta_c(h) = \delta_e(h)^{-1}$ and therefore $d_{\mathcal{M}}(h(\mathbf{x}_i), h(\mathbf{x}_j)) = \tau d_{\mathcal{G}}(i, j)$ for some $\tau > 0$ and all $i \neq j$. In simpler terms, an *embedding without distortion is a global similarity*, i.e., it globally scales pairwise distances in \mathcal{G} by a factor τ . The stricter case of a (global) isometry is obtained by requiring $\delta_e(h) = \delta_c(h) = 1$. Hyperbolic embeddings of trees can achieve arbitrarily low distortion under appropriate constructions (Sarkar, 2011). This motivates our first key question for hyperbolic message passing: *even if low-distortion hyperbolic embeddings exist, can a hyperbolic GNN actually learn them under supervision?*

3.1. Pairwise Distance Prediction: training explicitly for metric preservation

To address this question, we introduce a controlled synthetic task named the Pairwise Distance Prediction (PDP) task. Given a finite, connected graph $\mathcal{G} = (\mathcal{V}, \mathcal{E})$ we consider all node pairs $\mathcal{P} \subseteq \{(i, j) \in \mathcal{V} \times \mathcal{V} : i \neq j\}$, divide them in training, validation and test sets and define regression targets $D_{ij} := d_{\mathcal{G}}(i, j)$, $(i, j) \in \mathcal{P}$. We train the encoder h_{ϕ} to map nodes to a latent manifold $\mathbf{z}_i = h_{\phi}(\mathbf{x}_i) \in \mathcal{M}$, where \mathbf{x}_i are the features of node i and \mathcal{M} is either \mathbb{R}^d or $\mathcal{B}_c^d / \mathcal{L}_c^d$. For each pair we compute the corresponding latent distance $\hat{d}_{ij} = d_{\mathcal{M}}(\mathbf{z}_i, \mathbf{z}_j)$ and use it to predict D_{ij} through a scalar decoder $\hat{D}_{ij} = g_{\psi}(\hat{d}_{ij}) = a \hat{d}_{ij} + b$, $(i, j) \in \mathcal{P}$, where $\psi = (a, b)$. This isolates the role of the *geometry of the embedding space*: the model succeeds only if shortest-path distances can be expressed (up to affine rescaling) as geodesic distances in \mathcal{M} .

Stress loss. We optimize the parameters ϕ, ψ by minimizing a distortion-aware objective inspired by metric multidimensional scaling (Canzar et al., 2024):

$$\mathcal{L}_{\text{stress}}(\phi, \psi) = \frac{1}{|\mathcal{P}|} \sum_{(i, j) \in \mathcal{P}} \frac{(\hat{D}_{ij} - D_{ij})^2}{D_{ij}^2 + \varepsilon}, \quad (6)$$

where $\varepsilon > 0$ is a small constant for numerical stability. The normalization by D_{ij}^2 prevents optimization from being dominated by large-distance pairs. Importantly, driving this loss to zero operationalizes the goal of learning low-distortion (metric-preserving) representations. If this loss is further normalized by the stress obtained from a feature-only baseline that calculates distances directly in the input feature space, we refer to it as *Normalized Stress Loss*.

Datasets. To evaluate the PDP task, we construct two synthetic graphs with comparable size but different intrinsic geometry: a *tree* and a *grid*. These are canonical settings where hyperbolic and Euclidean latent spaces are respectively well matched. The *tree* is a balanced b -ary tree with branching factor $b = 5$ and depth $l = 4$ ($|\mathcal{V}| = 781$), whereas the *grid* is a 28×28 2D lattice ($|\mathcal{V}| = 784$). Node features are sparse (10%) Gaussian vectors in \mathbb{R}^{100} .

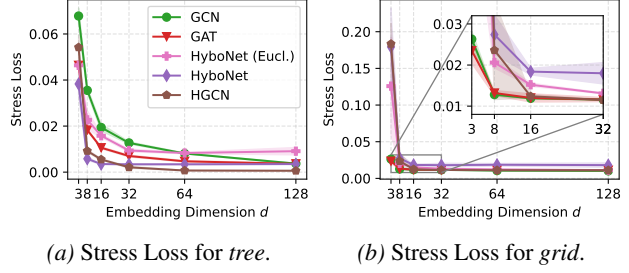


Figure 2. Test Stress Loss (\downarrow) as a function of the embedding dimension for the PDP task on the synthetic *tree* and *grid* graphs. Each marker denotes the mean performance over 10 random seeds; shaded regions indicate one standard deviation.

3.1.1. RESULTS

Results on the *tree* and *grid* graphs are reported in Fig. 2, with detailed values provided in Appendix F.1. All results are averaged over 10 random seeds. Inspired by Nash’s (1956) embedding theorems, we vary the embedding dimension d to assess whether Euclidean models can increasingly approximate a low-distortion embedding of the input graph. To isolate the role of geometry, we further compare HyboNet with a Euclidean counterpart that shares the same message-passing architecture and model capacity, differing only in the embedding space.

On the *tree*, hyperbolic models achieve substantially lower stress than Euclidean baselines at low dimensions, confirming that negative curvature provides an effective inductive bias for compactly representing trees. HyboNet performs best at $d = 3$, while HGCN becomes competitive at higher dimensions. As d increases, Euclidean models progressively close the gap, and by $d = 128$ all methods achieve comparable stress.

On the *grid*, the trend reverses: Euclidean models consistently achieve lower stress across all dimensions, indicating that flat geometry better matches grid distances. Notably, HGCN outperforms HyboNet in this setting, suggesting that its learnable curvature allows it to adapt toward an effectively Euclidean regime, whereas HyboNet operates with fixed curvature that is less suited to grid structure.

We complement the stress-based evaluation with another qualitative experiment that explicitly confronts pairwise distances in data versus embedding space. To do this we plot the averaged pairwise distances in latent space conditioned on the true graph distances. Then we perform a linear fit on these points and we report the R^2 score. Full results, along with a target-permutation control experiment verifying that observed gains are not driven by spurious correlations, are reported in Appendix F.1.

Key Takeaway

When supervision demands metric faithfulness, message passing can exploit the geometric inductive bias of the latent space. Hyperbolic architectures minimize distortion more effectively on hyperbolic inputs, especially at low dimensions where capacity is limited.

4. From Metric Preservation to Task-Aligned Geometry

Section 3 established an important result: *when supervision explicitly demands metric faithfulness*, hyperbolic message passing can recover optimal representations of tree-like graphs in terms of distortion. This dependence on supervision is clear from the control experiment in Appendix F.1: keeping the *tree* as input but randomly shuffling the targets breaks the link between labels and geometry, and hyperbolic models no longer outperform Euclidean ones. This leads us to the key claim of our study: *input hyperbolicity alone is not sufficient to justify HGNNS*, in contrast to the common existing belief. Instead, a hyperbolic inductive bias is beneficial precisely when it is aligned in some way with the geometric structure required by the task.

This raises the central question of this section: *when does a task require preserving (parts of) the input geometry?* To answer it, we now turn to a theoretical analysis grounded in geometry–task alignment. The simplest setting for this analysis is univariate *node regression* (NR), where the label space has metric $d_Y(y_i, y_j) = |y_i - y_j|$. This will allow us to quantify how geometric inductive biases are “inherited”.

We will now outline several assumptions in decreasing order of strength that relate the label and data geometries. The goal is to formalize the intuition that the labels inherit the input geometry if they share similar metric characteristics to the input graph. More specifically, we propose the following characterizations. Suppose that there exist constants $\alpha, \beta > 0$ such that for all $i, j \in \mathcal{V}$, $i \neq j$ such that:

$$(i) [\text{Global}] \alpha d_{\mathcal{G}}(i, j) \leq d_Y(y_i, y_j) \leq \beta d_{\mathcal{G}}(i, j).$$

$$(ii) [\text{Monotone Global}] \text{ there also exists a strictly increasing function } \omega : \mathbb{R} \rightarrow \mathbb{R} \text{ for which:}$$

$$\alpha d_{\mathcal{G}}(i, j) \leq d_Y(\omega(y_i), \omega(y_j)) \leq \beta d_{\mathcal{G}}(i, j).$$

$$(iii) [\text{Local}] \text{ nodes in an } r\text{-ball } d_{\mathcal{G}}(i, j) \leq r \text{ respect:}$$

$$\alpha d_{\mathcal{G}}(i, j) \leq d_Y(y_i, y_j) \leq \beta d_{\mathcal{G}}(i, j) \leq \beta r.$$

Now, consider the supervised problem of learning representations, with n_t training labels $\mathbf{y} = \{y_i\}_{i=1}^{n_t} \in \mathbb{R}^{n_t}$ and features $\mathbf{X} = \{\mathbf{x}_i\}_{i=1}^n \in \mathbb{R}^{n \times d'}$, which live upon a simple,

finite, and connected graph $\mathcal{G} = (\mathcal{V}, \mathcal{E})$, $|\mathcal{V}| = n$. The graph can be represented by a binary and symmetric adjacency matrix $\mathbf{A} \in \{0, 1\}^{n \times n}$, with $\mathbf{A}_{ij} = 1$ if $(i, j) \in \mathcal{E}$ and 0 otherwise. The learning problem consists in learning a model $f_{\theta}(\mathbf{x}_i, \mathcal{G}) = \hat{y}_i \in \mathbb{R}$ such that the prediction error $\frac{1}{2}(y_i - \hat{y}_i)^2$ is minimal over training instances. Unless noted otherwise, the representation manifolds are assumed to be Riemannian submanifolds in a Euclidean ambient space, therefore $\langle \cdot, \cdot \rangle$ and $\|\cdot\|$ correspond to the dot-product and Euclidean norm, respectively. The proofs of all statements are deferred to Appendix C.

Theorem 4.1. *Let $\mathcal{G} := (\mathcal{V}, \mathcal{E})$ be the input graph, $f = g \circ h$ be the model, with h an embedding as in Def. 3.1, and $g(\mathbf{z}_i | \mathbf{w}, b) : \mathcal{M} \rightarrow \mathbb{R}$ the solver, such that $\mathbf{z}_i = h(\mathbf{x}_i) \rightarrow \langle \mathbf{w}, \mathbf{z}_i \rangle + b = y_i$. Define the quantities:*

$$\xi(h) = \min_{i, j \in \mathcal{V}, i \neq j} \frac{\|h(\mathbf{x}_i) - h(\mathbf{x}_j)\|}{d_{\mathcal{M}}(h(\mathbf{x}_i), h(\mathbf{x}_j))}, \quad (7)$$

$$\zeta(h) = \max_{i, j \in \mathcal{V}, i \neq j} \frac{\|h(\mathbf{x}_i) - h(\mathbf{x}_j)\|}{d_{\mathcal{M}}(h(\mathbf{x}_i), h(\mathbf{x}_j))}, \quad (8)$$

$$\rho(h, \mathbf{w}) = \min_{i, j \in \mathcal{V}} \frac{|\langle \mathbf{w}, h(\mathbf{x}_i) - h(\mathbf{x}_j) \rangle|}{\|\mathbf{w}\| \|h(\mathbf{x}_i) - h(\mathbf{x}_j)\|}. \quad (9)$$

Then, if $\rho(h, \mathbf{w}) > 0$, f is bi-Lipschitz onto its image with upper constant $\beta = \|\mathbf{w}\| \zeta(h) \delta_e(h)$ and lower constant $\alpha = \frac{\|\mathbf{w}\| \xi(h) \rho(h, \mathbf{w})}{\delta_c(h)}$, such that $\alpha d_{\mathcal{G}}(i, j) \leq |y_i - y_j| \leq \beta d_{\mathcal{G}}(i, j)$.

Here we describe a global dependency, but it is possible to consider any of three alignment types presented previously to specialize it to cases of interest. To gain more insight on geometry–task alignment from Thm. 4.1, we define the concept of model distortion:

Definition 4.2 (Model distortion). *Let \mathcal{G} be the input graph, f be the model, and β, α the upper and lower constants following Thm. 4.1. The model distortion is defined as the condition number $k(f) = \frac{\beta}{\alpha} = \frac{\zeta(h) \delta_e(h)}{\xi(h) \rho(h, \mathbf{w})}$.*

Intuitively, the model distortion acts similarly to the embedding distortion defined in Def. 3.1 for the complete learning model, in that a value of 1 indicates a rescaling of the pairwise distances from data space to label space. Most importantly, it provides insights into Thm 4.1, showing how we can understand the alignment between task and geometry as being proportional to embedding distortion, but also local deviation from the ambient space where the solver operates.

Proposition 4.3 (Euclidean embeddings). *Let \mathcal{G} be the input graph, f be the model, h the embedding function, and g the solver function, all as defined in Thm. 4.1. Furthermore, let h be an embedding of the graph into Euclidean space \mathbb{R}^d . The model distortion of f is*

$$k(f) = \frac{\delta(h)}{\rho(h, \mathbf{w})}. \quad (10)$$

We can see that in the most practically employed case of learning Euclidean embeddings, the model distortion and thus the geometry–task relationship is directly proportional to the distortion of the embedding function. By making the assumption of non-orthogonality between any chord in representation space and the weight vector of g , the model distortion is in fact no less than the embedding distortion, given that $0 < \rho(h, \mathbf{w}) \leq 1 \implies k(f) \geq \delta(h)$. This fact is precisely the intuition behind most papers that propose the use of HGNNs for tree-like graphs (Chami et al., 2019). The following propositions show that despite being intuitive, this motivation is not always necessarily optimal.

Proposition 4.4 (Similarities and isometries). *Let \mathcal{G} be the input graph, f be the model, h the embedding function, and g the solver function, all as defined in Thm. 4.1. If $\delta(h) = 1$, the model distortion of f is*

$$k(f) = \frac{\zeta(h)}{\xi(h)\rho(h, \mathbf{w})}. \quad (11)$$

Proposition 4.5 (Poincaré ball embeddings). *Let \mathcal{G} be the input graph, f be the model, h the embedding function, and g the solver function, all as defined in Thm. 4.1. Let h be an embedding function that embeds the Poincaré ball \mathcal{B}_1^d and define $\eta := \max_{i \in \mathcal{V}} \|h(\mathbf{x}_i)\|$. Then, the model distortion of f is*

$$k(f) = \frac{\delta(h)}{(1 - \eta^2)\rho(h, \mathbf{w})}. \quad (12)$$

From this result we can see that the geometry–task alignment capabilities of the model are controlled by an interesting trade-off. Prop. 4.4 shows that for a model whose embedding function is a similarity or isometry, the resulting alignment depends on how much the representation space deviates from Euclidean space. This is because the solver operates in the ambient space, therefore the intuition is that if the representation space is excessively curved, the model distortion will increase. Prop. 4.5 puts this into concrete perspective: If points are too close to the boundary, the hyperbolic distance tends to be infinite, which makes it difficult to provide tight alignment bounds for the linear solver. So, if the embedding distortion is $\delta(h) = 1$, the sole geometric price to pay is how close you get to the boundary, which is in direct relationship with the curvature.

Note that this has been observed empirically for hyperbolic generative models (Wen et al., 2024), where typically the curvature of the latent space is set close to 0. In the context of the statements above, this gives the model “more space” before getting to the boundary, which, combined with the fact that close to the origin distances deviate only slightly from Euclidean ones, can lead to better learning.

Table 1. NR MAE (\downarrow) on the synthetic tree and grid dataset for dimension 3 and ≤ 128 , and control on the tree.

MODEL	TREE			GRID	
	3	≤ 128	CONTROL	3	≤ 128
MLP	1.24 \pm 0.06	1.20 \pm 0.06	1.20 \pm 0.07	8.36 \pm 1.67	9.40 \pm 2.67
GCN	0.51 \pm 0.24	0.47 \pm 0.24	1.19 \pm 0.07	0.45 \pm 0.10	0.46 \pm 0.04
GAT	0.63 \pm 0.39	0.21 \pm 0.13	1.21 \pm 0.05	0.41\pm0.14	0.29 \pm 0.06
HYBONET	0.17\pm0.02	0.07\pm0.02	1.23 \pm 0.06	1.85 \pm 0.55	0.45 \pm 0.08
HGCN	0.25 \pm 0.05	0.08 \pm 0.02	1.16\pm0.06	0.44 \pm 0.07	0.27\pm0.06

4.1. Experiments on Node Regression

In order to have a controlled setting where we can verify our theoretical results, we propose a simple task. Suppose we are given a graph \mathcal{G} with n nodes. We can extract an anchor node $a \in V$ and define a label for each node $i \in V \setminus \{a\}$ as $y_i = \beta^* d_{\mathcal{G}}(i, a)$, for $\beta^* > 0$. Using the reverse triangle inequality and excluding a from the labeled set, we have

$$\begin{aligned} 0 \leq |y_i - y_j| &= \beta^* |d_{\mathcal{G}}(i, a) - d_{\mathcal{G}}(a, j)| \\ &\leq \beta^* d_{\mathcal{G}}(i, j). \end{aligned} \quad (13)$$

Concretely, we use a synthetic tree with depth $l = 4$ and branching factors $b = (100, 2, 2, 2)$, equipped with sparse (10%) Gaussian features in \mathbb{R}^{100} . The target label is the distance to the root, so the regression error reflects geometric alignment by testing whether the model captures the exponential expansion of the underlying space. As a sanity check, we also report results for a target-permutation baseline under the control column. To assess alignment on a non-hyperbolic structure, we consider the same grid graph as in Section 3.1, using a central node as anchor. We evaluate the same models as in Section 3, along with an MLP. Models are tested in two configurations: a constrained setting with dimension 3, and the best configuration among $\{16, 32, 64, 128\}$ (denoted by ≤ 128). Performance is measured using Mean Absolute Error (MAE) over 10 splits.

4.1.1. RESULTS

The results in Table 1 show that all GNNs perform significantly better than the MLP on both datasets, verifying that the graph structure is crucial to the problem. On the tree graph, the fully hyperbolic HyboNet clearly outperforms all other methods. We conjecture that this is because HyboNet operates completely in hyperbolic space and has no issues with the ambient solver alignment. On the other hand HGCN performs slightly worse than HyboNet, because of the error induced by the Euclidean linear decoder (Prop. 4.5).

We empirically verify this trade-off by plotting the MAE as a function of the curvature parameter in Figure 3. For a fixed curvature magnitude of $c = 0.1$ and the same hyperparameters, HGCN outperforms all other methods except HyboNet. These phenomena are even more pronounced when working

in low dimensional spaces ($d = 3$). On the other hand, Euclidean models work better on the grid. HGCN is able to keep up due to its learnable curvature parameter, while HyboNet performs worst among all GNN methods for a small embedding dimension. Taking into account the control experiment, where all methods perform the same, these results indicate that it is not sufficient for general tasks to consider δ -hyperbolicity, but also the preservation of geometry that the tasks requires.

Finally, our analysis suggests that NR can be a natural setting where hyperbolic advantages *should* emerge; yet, to the best of our knowledge, NR has not been used as a standard benchmark in prior work on HGNNs, likely due to the lack of established tree-like NR benchmarks. We therefore highlight this as an important direction for future work.

Key Takeaway

When NR is geometry-aligned on tree-like graphs, fully hyperbolic methods outperform others. Methods that rely on tangent space computations might degrade in performance if the space considered is strongly curved, so this parameter must be controlled.

5. Real-World Tasks: Node Classification and Link Prediction

We now evaluate whether HGNNs provide an advantage over Euclidean ones on the standard real-world benchmarks used in the HGNN literature, focusing on the canonical tasks of node classification (NC) and link prediction (LP) across Disease, Airport, Cora, Pubmed, and Citeseer. In all experiments, we report mean \pm std. over 10 splits. We recompute the Gromov δ -hyperbolicity exactly using SageMath (Stein & Joyner, 2005) rather than via approximation (see Appendix D).

5.1. Node Classification

We consider two complementary aspects on the same standard datasets: the usual predictive performance metrics (Macro F1, Accuracy) to assess whether HGNNs yield an empirical advantage over Euclidean counterparts and we directly analyze the geometry of the learned representations. Concretely, after the end-to-end training of each model for

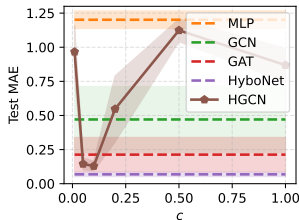
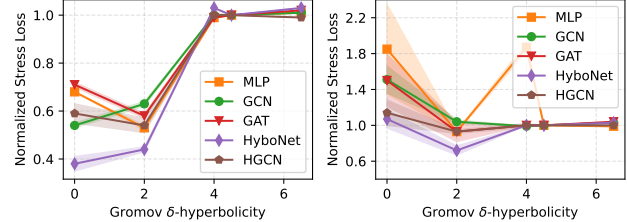


Figure 3. NR MAE (↓) of HGCN vs. its fixed curvature magnitude c on the tree for $d = 128$. We can see a curvature–performance trade-off.



(a) Real-world LP Stress Loss. (b) Real-world NC Stress Loss.

Figure 4. Normalized Stress loss (↓) for predicting pairwise shortest-path distances using embeddings from LP (a) and NC (b). Hyperbolic models perform best for LP at small δ , while gains for NC are marginal.

classification, we measure how faithfully the learned node representations preserve the input graph metric via the stress loss (Section 3). Details on the split and on the experimental setup are reported in Appendix E. Importantly, compared to prior work, we fixed bugs in the data splitting of Disease (indicated by *) and a data leakage issue in Airport.

5.1.1. RESULTS

The results are reported in the right half of Table 2. Across all benchmarks, including the most tree-like ones (Disease and Airport), HGNNs do not provide significant improvements over Euclidean counterparts, as also reflected by the Absolute Gain values. This is consistent with our geometry–task alignment perspective. In NC, the label space is discrete and permutation-invariant, and there is no meaningful notion of distance between classes (e.g., class 1 is not “closer” to class 2 than to class 3). As a result, the task does not induce a notion of metric preservation. This can also be seen as a direct result of learning to minimize the usual cross-entropy objective, which promotes the collapse of representations (Parker et al., 2023): it is sufficient to cluster class embeddings, without any structural ordering between classes. This intuition is further supported by the evidence of the distortion analysis in Fig. 4b. When trained for classification, none of the methods learn embeddings that faithfully preserve shortest-path distances, *no matter how hyperbolic the input graphs are*. In other words, classification favors class separability over global metric faithfulness.

Key Takeaway

For NC, HGNNs offer no consistent advantage over Euclidean models, even on tree-like graphs, since the task does not require preserving the input metric and instead encourages class-wise representation collapse.

Table 2. LP (ROC AUC \uparrow) and NC (Macro F1 \uparrow) results on real-world datasets. We also report Gromov δ -hyperbolicity (lower is more hyperbolic). The last row shows the Absolute Gain of the best hyperbolic model over the best Euclidean GNN model.

MODEL	LINK PREDICTION (LP)					NODE CLASSIFICATION (NC)				
	DISEASE $\delta = 0$	AIRPORT $\delta = 2$	CORA $\delta = 4$	PUBMED $\delta = 4.5$	CITESEER $\delta = 6.5$	DISEASE* $\delta = 0$	AIRPORT $\delta = 2$	CORA $\delta = 4$	PUBMED $\delta = 4.5$	CITESEER $\delta = 6.5$
MLP	98.43 \pm 0.74	97.66 \pm 0.12	90.33 \pm 0.94	94.52 \pm 0.26	91.45 \pm 0.68	48.62 \pm 5.06	88.79 \pm 1.97	55.63 \pm 1.50	70.45 \pm 1.12	54.29 \pm 1.14
GCN	91.67 \pm 1.79	96.58 \pm 0.35	92.98 \pm 1.01	95.03 \pm 0.19	96.02 \pm 0.50	89.50 \pm 4.82	92.46 \pm 0.86	80.09 \pm 1.01	78.49 \pm 1.47	64.95 \pm 1.50
GAT	93.25 \pm 1.59	95.67 \pm 0.33	93.50 \pm 0.68	96.77 \pm 0.18	93.32 \pm 0.92	85.71 \pm 5.50	88.33 \pm 5.73	80.71 \pm 1.22	78.44 \pm 1.88	65.16 \pm 1.48
HYBONET	97.99 \pm 0.72	98.15 \pm 0.17	93.70 \pm 0.58	97.08 \pm 0.09	91.53 \pm 1.40	90.48 \pm 5.12	90.87 \pm 1.10	78.72 \pm 1.01	78.33 \pm 1.97	62.98 \pm 1.48
HGCN	95.16 \pm 2.50	97.66 \pm 0.15	93.88 \pm 1.09	96.86 \pm 0.11	94.46 \pm 0.61	90.51 \pm 3.45	90.92 \pm 2.04	78.34 \pm 0.95	78.21 \pm 1.47	63.29 \pm 2.07
ABS. GAIN	+4.74	+1.57	+0.38	+0.31	-1.56	+1.01	-1.54	-1.99	-0.16	-1.87

5.2. Link Prediction

For LP we consider the usual predictive performance metrics (ROC AUC, AP) and also the stress loss of the final embedding. As in prior work, all models use a distance-based decoder on the final embeddings to focus on the effects of latent geometry. Motivated by the analysis of Katsman & Gilbert (2025), which highlights that many commonly used LP benchmarks can be solved using node features alone via a simple MLP, we additionally consider controlled synthetic settings to disentangle feature-driven performance from structural advantages. Specifically, we progressively corrupt node features in highly δ -hyperbolic datasets (Disease and Airport) by injecting Gaussian noise, thereby degrading feature information. In Appendix F.2, we also evaluate on the synthetic $Tree1111_\gamma$ dataset of Katsman & Gilbert (2025). Full details on data splits and experimental setup are provided in Appendix E.

5.2.1. RESULTS

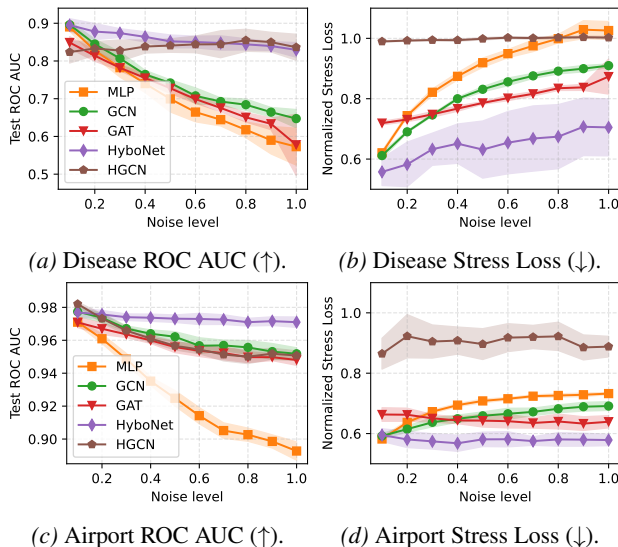


Figure 5. LP ROC AUC (\uparrow) (a, c) and Normalized Stress Loss (\downarrow) (b, d) over different noise levels added to the features of the Disease and Airport datasets. HyboNet outperforms all other methods in terms of ROC AUC and it does so by better preserving the geometry as measured by the Stress Loss.

The LP results on real-world datasets are shown in the left half of Table 2. HGNNs outperform Euclidean counterparts on the most tree-like datasets (Disease and Airport), while on the remaining benchmarks all GNNs achieve very similar ROC AUC. This trend is shown by the absolute gain, which is strongly positive on low- δ graphs and close to zero (or negative) elsewhere. These results align with the view of LP as a *geometry-aligned* problem: predicting edges is tightly connected to *local* graph neighborhoods, and thus benefits from latent spaces that preserve graph structure in tree-like regimes. This is consistent with the stress analysis: on Disease and Airport, all message-passing models reduce stress compared to feature-only baselines, but HyboNet consistently achieves the lowest values, indicating the strongest preservation of input geometry. Interestingly, on Disease and Airport the MLP baseline can match or even exceed GNN performance, which is due to the fact that standard LP splits can fragment tree-like graphs into many small components, limiting the usefulness of message passing and making strong node features sufficient (Bechler-Speicher et al., 2024). To isolate the contribution of structure, we progressively corrupt node features with Gaussian noise. As features become less informative (Fig. 5), GNNs outperform MLP, and hyperbolic models, especially HyboNet, maintain higher ROC AUC across noise levels. The same trend appears in the stress analysis (Fig. 5b/5d): increasing noise degrades metric preservation for all methods, while HyboNet remains stable and shows the lowest distortion.

Finally, these results highlight an important consideration: while LP is related to pairwise metric preservation, it does *not* require full global faithfulness. If an embedding perfectly preserved the entire graph metric, adjacency could be recovered from distances alone. However, LP imposes a weaker requirement: it is sufficient to separate node pairs at graph distance one from those at distance greater than one.

Key Takeaway

LP is inherently geometry-aligned: deciding whether two nodes are connected depends on their relative proximity in the input graph. HGNNs are therefore most effective on low- δ graphs.

6. Conclusion

We revisit when hyperbolic inductive biases are truly beneficial for GNNs and show that input hyperbolicity alone is insufficient: gains arise only when the task is aligned with the graph’s metric structure. We suggest that HGNNs are effective for link prediction on tree-like graphs, where geometry is inherently task-aligned, but provide no advantage for node classification, even in highly hyperbolic graphs, where separability dominates over geometric faithfulness. We also identify node regression as a promising yet under-explored setting, limited by the lack of suitable hyperbolic benchmarks. Overall, our results offer concrete guidance for practitioners and position geometry–task alignment as a principled criterion for model selection and future research. For future work, we aim to develop quantitative criteria for selecting hyperbolic models based on geometry–task alignment.

Impact Statement

This paper presents work whose goal is to advance the field of machine learning. There are many potential societal consequences of our work, none of which we feel must be specifically highlighted here.

Acknowledgments

D.N. and N.T. were supported by the BRAINFEDERATION FISA-2022-00899, by NEXGENERATIONEU (NGEU) and funded by the Italian Ministry of University and Research (MUR), National Recovery and Resilience Plan (NRRP), project MNESYS (PE0000006) (to NT)- A Multi-scale integrated approach to the study of the nervous system in health and disease (DN. 1553 11.10.2022); by the MUR-PNRR M4C2I1.3 PE6 project PE00000019 Heal Italia (to NT); by the NATIONAL CENTRE FOR HPC, BIG DATA AND QUANTUM COMPUTING, within the spoke “Multi-scale Modeling and Engineering Applications” (to NT); the EXPERIENCE project (European Union’s Horizon 2020 Research and Innovation Programme under grant agreement No. 101017727); the CROSSBRAIN project (European Union’s European Innovation Council under grant agreement No. 101070908; The BRAINSTORM PROJECT under Grant Agreement number 101099355.

References

Baker, C., Suárez-Méndez, I., Smith, G., Marsh, E. B., Funke, M., Mosher, J. C., Maestú, F., Xu, M., and Pantazis, D. Hyperbolic graph embedding of meg brain networks to study brain alterations in individuals with subjective cognitive decline. *IEEE journal of biomedical and health informatics*, 28(12):7357–7368, 2024.

Bechler-Speicher, M., Amos, I., Gilad-Bachrach, R., and Globerson, A. Graph neural networks use graphs when they shouldn’t. In *Proceedings of the 41st International Conference on Machine Learning*, ICML’24. JMLR.org, 2024.

Bécigneul, G. and Ganea, O.-E. Riemannian adaptive optimization methods. In *International Conference on Learning Representations*, 2019.

Benedetti, R. and Petronio, C. *Lectures on hyperbolic geometry*. Springer Science & Business Media, 1992.

Bonk, M. and Schramm, O. Embeddings of gromov hyperbolic spaces. In *Selected Works of Oded Schramm*, pp. 243–284. Springer, 2011.

Canzar, S., Do, V. H., Jelić, S., Laue, S., Matijević, D., and Prusina, T. Metric multidimensional scaling for large single-cell datasets using neural networks. *Algorithms for molecular biology*, 19(1):21, 2024.

Chami, I., Ying, Z., Ré, C., and Leskovec, J. Hyperbolic graph convolutional neural networks. *Advances in neural information processing systems*, 32, 2019.

Chami, I., Wolf, A., Juan, D.-C., Sala, F., Ravi, S., and Ré, C. Low-dimensional hyperbolic knowledge graph embeddings. In *Proceedings of the 58th Annual Meeting of the Association for Computational Linguistics*, pp. 6901–6914, 2020.

Chen, W., Han, X., Lin, Y., Zhao, H., Liu, Z., Li, P., Sun, M., and Zhou, J. Fully hyperbolic neural networks. In *Proceedings of the 60th Annual Meeting of the Association for Computational Linguistics (Volume 1: Long Papers)*, pp. 5672–5686, 2022.

Chepoi, V., Dragan, F. F., Estellon, B., Habib, M., Vaxes, Y., and Xiang, Y. Additive spanners and distance and routing labeling schemes for hyperbolic graphs. *Algorithmica*, 62(3):713–732, 2012.

Cohen, N., Coudert, D., and Lancin, A. *Exact and approximate algorithms for computing the hyperbolicity of large-scale graphs*. PhD thesis, INRIA, 2012.

Coudert, D., Nusser, A., and Viennot, L. Hyperbolicity computation through dominating sets. In *ALENEX 2022-SIAM Symposium on Algorithm Engineering and Experiments*, pp. 78–90, 2022.

Ganea, O., Bécigneul, G., and Hofmann, T. Hyperbolic neural networks. *Advances in neural information processing systems*, 31, 2018.

Greene, C. S., Krishnan, A., Wong, A. K., Ricciotti, E., Zelaya, R. A., Himmelstein, D. S., Zhang, R., Hartmann,

B. M., Zaslavsky, E., Sealfon, S. C., et al. Understanding multicellular function and disease with human tissue-specific networks. *Nature genetics*, 47(6):569–576, 2015.

Gromov, M. Hyperbolic groups. In *Essays in group theory*, pp. 75–263. Springer, 1987.

Grover, A. and Leskovec, J. node2vec: Scalable feature learning for networks. In *Proceedings of the 22nd ACM SIGKDD international conference on Knowledge discovery and data mining*, pp. 855–864, 2016.

Hamilton, W. L., Ying, R., and Leskovec, J. Inductive representation learning on large graphs. In *Advances in Neural Information Processing Systems (NeurIPS)*, 2017.

Hu, W., Fey, M., Zitnik, M., Dong, Y., Ren, H., Liu, B., Catasta, M., and Leskovec, J. Open graph benchmark: Datasets for machine learning on graphs. *Advances in neural information processing systems*, 33:22118–22133, 2020.

Katsman, I. and Gilbert, A. Shedding light on problems with hyperbolic graph learning. *Transactions on Machine Learning Research*, 2025. ISSN 2835-8856. Reproducibility Certification.

Katsman, I., Chen, E., Holalkere, S., Asch, A., Lou, A., Lim, S. N., and De Sa, C. M. Riemannian residual neural networks. *Advances in Neural Information Processing Systems*, 36:63502–63514, 2023.

Khoshrafter, S. and An, A. A survey on graph representation learning methods. *ACM Transactions on Intelligent Systems and Technology*, 15(1):1–55, 2024.

Kingma, D. P. and Ba, J. Adam: A method for stochastic optimization. In *3rd International Conference on Learning Representations, ICLR 2015, San Diego, CA, USA, May 7-9, 2015, Conference Track Proceedings*, 2015.

Kipf, T. N. and Welling, M. Semi-supervised classification with graph convolutional networks. In *International Conference on Learning Representations*, 2017.

Kitsak, M., Voitalov, I., and Krioukov, D. Link prediction with hyperbolic geometry. *Physical Review Research*, 2(4):043113, 2020.

Kolivakis, P., Kalousis, A., and Kiritidis, D. Hyperbolic knowledge graph embeddings for knowledge base completion. In *European Semantic Web Conference*, pp. 199–214. Springer, 2020.

Krioukov, D., Papadopoulos, F., Kitsak, M., Vahdat, A., and Boguná, M. Hyperbolic geometry of complex networks. *Physical Review E—Statistical, Nonlinear, and Soft Matter Physics*, 82(3):036106, 2010.

Lee, J. M. *Riemannian manifolds: an introduction to curvature*, volume 176. Springer Science & Business Media, 2006.

Lee, J. M. *Introduction to Riemannian manifolds*, volume 2. Springer, 2018.

Li, Y., Zhang, X., Cui, Y., and Ma, S. Hyperbolic graph neural network for temporal knowledge graph completion. In *Proceedings of the 2024 Joint International Conference on Computational Linguistics, Language Resources and Evaluation (LREC-COLING 2024)*, pp. 8474–8486, 2024.

Liu, Q., Nickel, M., and Kiela, D. Hyperbolic graph neural networks. *Advances in neural information processing systems*, 32, 2019.

Martelli, B. An introduction to geometric topology. *arXiv preprint arXiv:1610.02592*, 2016.

Matsumoto, H., Mimori, T., and Fukunaga, T. Novel metric for hyperbolic phylogenetic tree embeddings. *Biology Methods and Protocols*, 6(1):bpab006, 2021.

McAuley, J., Targett, C., Shi, Q., and van den Hengel, A. Image-based recommendations on styles and substitutes. In *Proceedings of the 38th International ACM SIGIR Conference on Research and Development in Information Retrieval, SIGIR ’15*, pp. 43–52, New York, NY, USA, 2015. Association for Computing Machinery. ISBN 9781450336215. doi: 10.1145/2766462.2767755.

Naddeo, D., Azevedo, T., and Toschi, N. Do we need curved spaces? a critical look at hyperbolic graph learning in graph classification. 2024.

Nash, J. The imbedding problem for riemannian manifolds. *Annals of mathematics*, 63(1):20–63, 1956.

Nickel, M. and Kiela, D. Poincaré embeddings for learning hierarchical representations. *Advances in neural information processing systems*, 30, 2017.

Nickel, M. and Kiela, D. Learning continuous hierarchies in the lorentz model of hyperbolic geometry. In *International conference on machine learning*, pp. 3779–3788. PMLR, 2018.

Pan, Z. and Wang, P. Hyperbolic hierarchy-aware knowledge graph embedding for link prediction. In *Findings of the Association for Computational Linguistics: EMNLP 2021*, pp. 2941–2948, 2021.

Papadopoulos, F., Krioukov, D., Boguná, M., and Vahdat, A. Greedy forwarding in dynamic scale-free networks embedded in hyperbolic metric spaces. In *2010 Proceedings IEEE Infocom*, pp. 1–9. IEEE, 2010.

Parker, L., Onal, E., Stengel, A., and Intrater, J. Neural collapse in the intermediate hidden layers of classification neural networks. *arXiv preprint arXiv:2308.02760*, 2023.

Pei, H., Wei, B., Chang, K. C.-C., Lei, Y., and Yang, B. Geom-gcn: Geometric graph convolutional networks. In *International Conference on Learning Representations*, 2020.

Perozzi, B., Al-Rfou, R., and Skiena, S. Deepwalk: Online learning of social representations. In *Proceedings of the 20th ACM SIGKDD international conference on Knowledge discovery and data mining*, pp. 701–710, 2014.

Platonov, O., Kuznedelev, D., Diskin, M., Babenko, A., and Prokhorenkova, L. A critical look at the evaluation of GNNs under heterophily: Are we really making progress? In *The Eleventh International Conference on Learning Representations*, 2023.

Ratcliffe, J. G. Hyperbolic n-manifolds. In *Foundations of Hyperbolic Manifolds*, pp. 506–596. Springer, 2019.

Ribeiro, L. F., Saverese, P. H., and Figueiredo, D. R. struc2vec: Learning node representations from structural identity. In *Proceedings of the 23rd ACM SIGKDD international conference on knowledge discovery and data mining*, pp. 385–394, 2017.

Rozemberczki, B. and Sarkar, R. Characteristic functions on graphs: Birds of a feather, from statistical descriptors to parametric models. In *Proceedings of the 29th ACM international conference on information & knowledge management*, pp. 1325–1334, 2020.

Rozemberczki, B., Allen, C., and Sarkar, R. Multi-Scale attributed node embedding. *Journal of Complex Networks*, 9(2):cnab014, 05 2021. ISSN 2051-1329. doi: 10.1093/comnet/cnab014.

Sarkar, R. Low distortion delaunay embedding of trees in hyperbolic plane. In *International symposium on graph drawing*, pp. 355–366. Springer, 2011.

Scarselli, F., Gori, M., Tsoi, A. C., Hagenbuchner, M., and Monfardini, G. The graph neural network model. *IEEE transactions on neural networks*, 20(1):61–80, 2008.

Sen, P., Namata, G., Bilgic, M., Getoor, L., Gallagher, B., and Eliassi-Rad, T. Collective classification in network data. *AI Mag.*, 29(3):93–106, 2008. ISSN 0738-4602. doi: 10.1609/aimag.v29i3.2157.

Shchur, O., Mumme, M., Bojchevski, A., and Günnemann, S. Pitfalls of graph neural network evaluation. *CoRR*, abs/1811.05868, 2018.

Shimizu, R., Mukuta, Y., and Harada, T. Hyperbolic neural networks++. In *International Conference on Learning Representations*, 2021.

Sonthalia, R. and Gilbert, A. Tree! i am no tree! i am a low dimensional hyperbolic embedding. *Advances in Neural Information Processing Systems*, 33:845–856, 2020.

Stein, W. and Joyner, D. Sage: system for algebra and geometry experimentation. *SIGSAM Bull.*, 39(2):61–64, June 2005. ISSN 0163-5824. doi: 10.1145/1101884. 1101889.

Tang, J., Sun, J., Wang, C., and Yang, Z. Social influence analysis in large-scale networks. In *Proceedings of the 15th ACM SIGKDD International Conference on Knowledge Discovery and Data Mining*, KDD ’09, pp. 807–816, New York, NY, USA, 2009. Association for Computing Machinery. ISBN 9781605584959. doi: 10.1145/1557019.1557108.

Veličković, P., Cucurull, G., Casanova, A., Romero, A., Liò, P., and Bengio, Y. Graph attention networks. In *International Conference on Learning Representations (ICLR)*, 2018.

Wang, X., Zhang, Y., and Shi, C. Hyperbolic heterogeneous information network embedding. In *Proceedings of the AAAI conference on artificial intelligence*, volume 33, pp. 5337–5344, 2019.

Wen, L., Tang, X., Ouyang, M., Shen, X., Yang, J., Zhu, D., Chen, M., and Wei, X. Hyperbolic graph diffusion model. In *Proceedings of the AAAI Conference on Artificial Intelligence*, volume 38, pp. 15823–15831, 2024.

Yang, M., Zhou, M., Li, Z., Liu, J., Pan, L., Xiong, H., and King, I. Hyperbolic graph neural networks: A review of methods and applications. *arXiv preprint arXiv:2202.13852*, 2022.

Yang, Y., Wu, L., Zhang, K., Hong, R., Zhou, H., Zhang, Z., Zhou, J., and Wang, M. Hyperbolic graph learning for social recommendation. *IEEE Transactions on Knowledge and Data Engineering*, 36(12):8488–8501, 2023.

Zhang, Y., Wang, X., Shi, C., Liu, N., and Song, G. Lorentzian graph convolutional networks. In *Proceedings of the web conference 2021*, pp. 1249–1261, 2021.

A. Related Works

Trees constitute a fundamental class of data structures. From a metric perspective, it is well established that trees are prototypical examples of negatively curved spaces. In his seminal work on hyperbolic groups, Gromov introduced the notion of δ -hyperbolicity (Gromov, 1987), formalizing hyperbolicity as a coarse, quasi-isometry-invariant property that depends only on large-scale geometry rather than local details or the choice of generating set (See Appendix D for computational details). In this sense, trees are 0-hyperbolic and share with hyperbolic spaces key global properties, including exponential volume growth.

Building on this perspective, Chepoi et al. (2012) showed that any n -node δ -hyperbolic graph admits a tree approximation with additive error $O(\delta \log n)$, demonstrating that tree metrics provide faithful approximations of distances in hyperbolic graphs. In the special case of trees themselves, Sarkar (2011) further strengthened this connection by providing a constructive embedding result: any weighted tree can be embedded into the two-dimensional hyperbolic plane with arbitrarily small distortion, preserving both topology and metric structure.

Real-world networks are rarely trees; however, many are approximately tree-like at large scales. This includes networks with scale-free degree distributions, where the probability $P(k)$ that a node has degree k follows a power law $P(k) \sim k^{-\gamma}$, with exponent γ typically between 2 and 3. Such networks often display strong heterogeneity, high clustering, and efficient navigability.

Krioukov et al. (2010) proposed a geometric framework in which these structural features arise naturally from an underlying hyperbolic geometry. In this model, degree heterogeneity is directly controlled by the negative curvature of the space, while clustering emerges as a consequence of its metric properties. Within the same framework, Papadopoulos et al. Papadopoulos et al. (2010) showed that scale-free network topologies naturally emerge from hyperbolic spaces and support efficient greedy routing based solely on geometric distances. Together, these results suggest that hyperbolic geometry provides a unifying explanation for the large-scale, tree-like organization observed in many real-world networks.

Rather than embedding a known tree, a complementary line of work aims to recover latent hierarchical structure directly from data by learning representations in hyperbolic space. Motivated by the exponential growth properties of hyperbolic geometry, these approaches leverage curvature as an inductive bias for modeling hierarchical organization. A seminal contribution in this direction was introduced by Nickel & Kiela (2017), who proposed Poincaré embeddings for learning continuous representations of symbolic data with latent hierarchies in an unsupervised setting, demonstrating substantial improvements over Euclidean embeddings. Building on this idea, Sonthalia & Gilbert (2020) proposed to first infer an approximate tree structure from the data and subsequently embed it into a low-dimensional hyperbolic space. Overall, these works bridge classical geometric embedding theory and modern representation learning, positioning hyperbolic space as a powerful tool for hierarchy induction rather than explicit metric reconstruction.

While hyperbolic space provides a powerful inductive bias for modeling hierarchical structure, learning in negatively curved spaces requires optimization techniques that go beyond standard Euclidean machinery. In particular, gradient-based learning must be generalized to Riemannian manifolds, where updates are performed along geodesics and parameters are constrained to remain on the manifold. Becigneul & Ganea (2019) addressed this challenge by extending popular adaptive optimization methods, including Adam and AdaGrad, to the Riemannian setting, providing both practical algorithms and theoretical guarantees. In parallel, the choice of the specific hyperbolic model was shown to have significant implications for numerical stability and computational efficiency. Nickel & Kiela (2018) demonstrated that learning embeddings in the Lorentz (hyperboloid) model is substantially more efficient than in the Poincaré ball, improving optimization behavior while preserving the representational advantages of hyperbolic geometry.

Building on advances in Riemannian optimization, hyperbolic geometry has been progressively integrated into standard neural architectures, enabling the transition from static embedding methods to fully trainable models. In this setting, core neural operations such as linear transformations, non-linearities, attention mechanisms, and residual connections are reformulated to operate directly in hyperbolic space while respecting its geometric constraints. Ganea et al. (2018) provided a foundational framework for hyperbolic neural networks by generalizing key components of deep learning to negatively curved manifolds. Subsequent work further expanded this paradigm, proposing unified formulations of neural network layers in the Poincaré ball (Shimizu et al., 2021) and extending residual architectures to general Riemannian manifolds in a principled manner (Katsman et al., 2023). Collectively, these contributions established hyperbolic neural networks as a viable and scalable modeling paradigm for learning hierarchical representations in an end-to-end fashion.

An active line of research has focused on extending GNNs to hyperbolic spaces in order to combine message passing with

the representational advantages of negative curvature. Two seminal works published in parallel in 2019 introduced the first hyperbolic GNN architectures (Liu et al., 2019; Chami et al., 2019). These approaches generalize Euclidean message passing by mapping node representations between hyperbolic space and local Euclidean tangent spaces via logarithmic and exponential maps. In particular, Chami et al. (2019) proposed an hyperbolic graph convolutional network with learnable curvature and attention mechanisms defined in hyperbolic space. Subsequent work sought to reduce reliance on tangent-space operations in order to better preserve geometric structure. Zhang et al. (2021) introduced a Lorentzian graph convolutional network that performs neighborhood aggregation directly in the hyperbolic manifold by computing centroids under the squared Lorentzian distance. Along similar lines, Chen et al. (2022) proposed a fully hyperbolic neural network operating entirely in the Lorentz model, demonstrating strong empirical performance on a range of benchmarks.

Despite the growing body of work on HGNNs, the benefits of hyperbolic message passing in supervised settings remain under active debate. Recently, Katsman & Gilbert (2025) provided a systematic reassessment of hyperbolic graph learning, highlighting several methodological issues related to baseline selection, modeling assumptions, and evaluation protocols. Notably, they showed that when Euclidean models with comparable capacity are carefully trained under the same experimental conditions, they often match or outperform existing hyperbolic graph representation learning methods, even on datasets previously characterized as highly hyperbolic according to Gromov hyperbolicity, including tree-structured graphs. Our work extends this reassessment by considering the interplay between representation geometry and task supervision, providing missing details on how the learning process might or might not require a geometric inductive bias that preserves the input metric structure.

B. Extended Background

B.1. Hyperbolic Geometry

In this section we provide more details on the exponential growth of (a model of) hyperbolic space and also the architectural mechanisms of HGNNs. For a more rigorous and detailed treatment of hyperbolic geometry and hyperbolic manifolds, we refer the reader to (Benedetti & Petronio, 1992; Martelli, 2016; Ratcliffe, 2019), while (Lee, 2018; 2006) are fantastic resources for the theory of Riemannian manifolds. For a general overview of hyperbolic graph learning and applications, please consult the review of Yang et al. (2022).

The Hyperboloid Model. To illustrate exponential volume growth, we consider (w.l.o.g) the hyperbolic space \mathcal{L}_c^d with unit negative curvature $c = -1$, which we will simply denote by \mathcal{L}^d .

Definition B.1 (Lorentzian scalar product). Let $u = (u_0, u_1, \dots, u_d)$ and $v = (v_0, v_1, \dots, v_d)$ be vectors in \mathbb{R}^{d+1} . The *Lorentzian scalar product* on \mathbb{R}^{m+1} is defined as

$$\langle u, v \rangle_{1,d} = -u_0 v_0 + \sum_{i=1}^d u_i v_i.$$

This bilinear form induces a pseudo-metric of signature $(1, d)$ on \mathbb{R}^{d+1} . We can now define an inner product space by equipping \mathbb{R}^{m+1} with the Lorentzian scalar product, called the $(d+1)$ -dimensional Minkowski space

$$\mathbb{R}^{1,d} = (\mathbb{R}^{d+1}, \langle \cdot, \cdot \rangle_{1,d}).$$

For any $x \in \mathbb{R}^{1,d}$ we define its *orthogonal complement* as

$$x^\perp = \{y \in \mathbb{R}^{1,d} : \langle x, y \rangle_{1,d} = 0\}.$$

We can now define the hyperboloid as the set of all points of norm -1 in the $(d+1)$ -dimensional Minkowski space. This set is a two-sheeted hyperboloid, and by restricting to the upper sheet to get the Lorentz model

$$\mathcal{L}^d = \{x = (x_0, \dots, x_d) \in \mathbb{R}^{1,d} : -x_0^2 + x_1^2 + \dots + x_d^2 = -1, x_0 > 0\}.$$

It is possible to show that \mathcal{L}^d is a differentiable manifold and, for every $x \in \mathcal{L}^d$, the tangent space $T_x \mathcal{L}^d$ coincides with x^\perp . For intuition about this fact, consider that the hyperboloid is an anti-sphere (a sphere of imaginary radius).

To define the metric on this manifold, we can use the notion of induced metric, also known as the first fundamental form. This simply consists in defining the Riemannian metric as the restriction of the ambient inner product to the tangent space:

$$g_x : T_x \mathcal{L}^d \times T_x \mathcal{L}^d \rightarrow \mathbb{R} \text{ s.t. } g_x(u, v) = \langle u, v \rangle_{1,d}, \quad u, v \in T_x \mathcal{L}^d$$

The induced metric provides the natural Riemannian metric which allows us to compute lengths, angles, and volumes in hyperbolic space. From this point forward, when we talk about \mathcal{L}^d , we actually refer to its Riemannian form, i.e., the tuple (\mathcal{L}^d, g) , where g is the induced metric described above. This is the *hyperboloid model* of hyperbolic space.

Exponential Growth of Volume. We compute the volume of a geodesic ball and show that it grows exponentially with the radius. To this end, we consider the parametrization

$$x(r, w) = (\cosh r, \sinh r w),$$

where $r \geq 0$ is the hyperbolic radius and $w \in S^{d-1} \subset \mathbb{R}^d$ provides the angular direction. It is immediate to check that the image of this parametrization lies in \mathcal{L}^d . For a clear exposition, let $\theta = \{\theta_1, \dots, \theta_{d-1}\} \in S^{d-1}$ be the local coordinates on the sphere, which implies we have a coordinate function $w = w(\theta)$. To compute the induced metric, we can just compute the metric components by considering the tangent basis in above coordinates

$$\partial_r x = (\sinh r, \cosh r w), \quad \partial_\theta x = (0, \sinh r \partial_\theta w).$$

The coefficients of the first fundamental form in the coordinates (r, w) are given, in Gauss notation, by

$$E = \langle \partial_r x, \partial_r x \rangle_{1,d}, \quad F = \langle \partial_r x, \partial_\theta x \rangle_{1,d}, \quad G = \langle \partial_\theta x, \partial_\theta x \rangle_{1,d}.$$

A direct computation yields

$$\begin{aligned} E &= -\sinh^2 r + \cosh^2 r = 1, \\ F &= 0, \\ G &= \sinh^2 r \|\partial_\theta w\|^2. \end{aligned}$$

Note that in the angular component of the metric G , we have the induced metric on the unit sphere $\|\partial_\theta w\|^2 = g_{S^{d-1}}$. We can now write the metric in matrix notation as

$$g = \begin{pmatrix} 1 & 0 \\ 0 & \sinh^2(r) g_{S^{d-1}} \end{pmatrix},$$

To obtain the Riemannian volume element, we simply scale the typical volume form by the factors induced by the metric, i.e., its determinant

$$\det g = \sinh^{2d-1} r \det(g_{S^{d-1}}),$$

and therefore in the coordinates (r, θ) the Riemannian volume element becomes

$$\sqrt{\det g} = \sinh^{d-1}(r) \sqrt{\det g_{S^{d-1}}}.$$

$$dV = \sqrt{\det g} dr d\theta_1 \cdots d\theta_{d-1}.$$

Since

$$\sqrt{\det g} = \sinh^{m-1}(r) \sqrt{\det g_{S^{d-1}}},$$

and the angular part can be written as

$$\sqrt{\det g_{S^{d-1}}} d\theta_1 \cdots d\theta_{d-1} = d\Omega_{d-1},$$

i.e., the standard volume element of the unit sphere, we obtain

$$dV = \sinh^{d-1}(r) dr d\Omega_{d-1}.$$

Integrating the volume element over a geodesic ball of radius R from the origin we obtain

$$\text{Vol}(B_R) = \int_{B_R} dV = \int_{S^{d-1}} \int_0^R \sinh^{d-1}(r) dr d\Omega_{d-1}.$$

Since the angular integral yields the area of the unit sphere S^{d-1} , denoted by $\omega_{d-1} = \text{Area}(S^{d-1})$, we arrive at

$$\text{Vol}(B_R) = \omega_{d-1} \int_0^R \sinh^{d-1}(r) dr.$$

As $r \rightarrow \infty$, by the exponential definition of sinh we have the asymptotic behavior

$$\sinh r \sim \frac{1}{2}e^r,$$

and consequently

$$\sinh^{d-1}(r) \sim 2^{-(d-1)}e^{(d-1)r},$$

which allows us to conclude that

$$\text{Vol}(B_R) \sim \frac{\omega_{d-1}}{(d-1)2^{d-1}} e^{(m-1)R}$$

It is therefore the case that the volume of geodesic balls in \mathcal{L}^d grows exponentially with rate $(m-1)$ in the radius R .

B.2. Hyperbolic Graph Learning

In this section, we review the GNN message-passing mechanism and provide an overview of standard hyperbolic GNN frameworks.

Graph Neural Networks. GNNs learn node representations through iterative neighborhood aggregation, providing an inductive alternative to transductive graph embeddings. Given initial node features $\mathbf{x}_v^{(0)} \in \mathbb{R}^{d'}$, representations are updated layer by layer via message passing:

$$\mathbf{m}_v^{(\ell)} = \text{AGG}^{(\ell)} \left(\{\mathbf{x}_u^{(\ell-1)} : u \in \mathcal{N}(v)\} \right), \quad (14)$$

$$\mathbf{x}_v^{(\ell)} = \text{UPD}^{(\ell)} \left(\mathbf{x}_v^{(\ell-1)}, \mathbf{m}_v^{(\ell)} \right), \quad (15)$$

where $\mathcal{N}(v)$ denotes the neighbors of node v , and AGG is a permutation-invariant function (e.g., sum, mean, or max). This formulation encompasses a broad class of Euclidean GNN architectures, including GCNs and GATs, which differ in their specific choices of aggregation and update functions.

HGNNs. Hyperbolic Graph Neural Networks (HGNNs) extend standard message passing to non-Euclidean geometries by learning node representations on hyperbolic manifolds. In this setting, node representations at layer ℓ are denoted by $\mathbf{z}_v^{(\ell)} \in \mathcal{H}_c^d$, where \mathcal{H}_c^d is a model of d -dimensional hyperbolic space with curvature $-c$ (e.g., \mathcal{B}_c^d or \mathcal{L}_c^d). The goal of HGNNs is to perform aggregation and transformation operations that are consistent with the underlying hyperbolic geometry. Existing approaches can be broadly grouped into two design families.

Tangent-space HGNNs perform message passing in Euclidean tangent spaces. Node representations are first mapped from the manifold to a tangent space via a logarithmic map, updated using standard GNN operations, and then mapped back to hyperbolic space via an exponential map. A representative example is HGCRN (Chami et al., 2019), which operates in the tangent space at a reference point, typically the origin \mathbf{o} :

$$\mathbf{x}_v^{(\ell-1)} = \log_{\mathbf{o}} \left(\mathbf{z}_v^{(\ell-1)} \right) \in T_{\mathbf{o}} \mathcal{H}_c^d, \quad (16)$$

$$\mathbf{x}_v^{(\ell)} = \text{UPD}^{(\ell)} \left(\mathbf{x}_v^{(\ell-1)}, \mathbf{m}_v^{(\ell)} \right), \quad (17)$$

$$\mathbf{z}_v^{(\ell)} = \exp_{\mathbf{o}} \left(\mathbf{x}_v^{(\ell)} \right) \in \mathcal{H}_c^d, \quad (18)$$

where the curvature c is in fact a learnable hyperparameter.

Fully HGNs instead aim to perform aggregation, transformation, and non-linear activation directly in hyperbolic space, avoiding explicit tangent-space projections. We consider HyboNet (Chen et al., 2022) as a representative of this class. HyboNet operates in the Lorentz model and combines linear transformation and non-linearity within a single hyperbolic layer. Given aggregated features $\mathbf{x}_v^{(\ell)}$, obtained via an attention-weighted center of mass in Lorentz space, the update is defined as

$$\mathbf{z}_v^{(\ell)} = \left[\begin{array}{c} \sqrt{\|\phi(\mathbf{W}\mathbf{x}_v^{(\ell)}, \mathbf{v})\|^2 - \frac{1}{c}} \\ \frac{\phi(\mathbf{W}\mathbf{x}_v^{(\ell)}, \mathbf{v})}{\|\phi(\mathbf{W}\mathbf{x}_v^{(\ell)}, \mathbf{v})\|} \end{array} \right], \quad (19)$$

where \mathbf{W} and \mathbf{v} are learnable parameters and $\phi(\cdot)$ denotes a non-linear transformation. This formulation ensures that updated representations remain on the Lorentz hyperboloid without having to use rely on the tangent space formalism.

C. Proofs

For the sake of clarity and exposition, we report here both the statements and their respective proofs. We remind the reader that in all the statements below, the representation manifolds are assumed to be Riemannian submanifolds in a Euclidean ambient space, therefore $\langle \cdot, \cdot \rangle$ and $\|\cdot\|$ correspond to the dot-product and Euclidean norm, respectively. We would like to note that this setting excludes the Lorentz model, but we can make considerations about the Poincaré model.

Theorem 4.1 Let $\mathcal{G} := (\mathcal{V}, \mathcal{E})$ be the input graph, $f = g \circ h$ be the model, with h an embedding as in Def. 3.1, and $g(\mathbf{z}_i|\mathbf{w}, b) : \mathcal{M} \rightarrow \mathbb{R}$ the solver, such that $\mathbf{z}_i = h(\mathbf{x}_i) \rightarrow \langle \mathbf{w}, \mathbf{z}_i \rangle + b = y_i$. Define the quantities:

$$\xi(h) = \min_{\substack{i, j \in \mathcal{V} \\ i \neq j}} \frac{\|h(\mathbf{x}_i) - h(\mathbf{x}_j)\|}{d_{\mathcal{M}}(h(\mathbf{x}_i), h(\mathbf{x}_j))}, \quad (20)$$

$$\zeta(h) = \max_{\substack{i, j \in \mathcal{V} \\ i \neq j}} \frac{\|h(\mathbf{x}_i) - h(\mathbf{x}_j)\|}{d_{\mathcal{M}}(h(\mathbf{x}_i), h(\mathbf{x}_j))}, \quad (21)$$

$$\rho(h, \mathbf{w}) = \min_{\substack{i, j \in \mathcal{V} \\ i \neq j}} \frac{|\langle \mathbf{w}, h(\mathbf{x}_i) - h(\mathbf{x}_j) \rangle|}{\|\mathbf{w}\| \|h(\mathbf{x}_i) - h(\mathbf{x}_j)\|}. \quad (22)$$

Then, if $\rho(h, \mathbf{w}) > 0$, f is bi-Lipschitz onto its image with upper constant $\beta = \|\mathbf{w}\| \zeta(h) \delta_e(h)$ and lower constant $\alpha = \frac{\|\mathbf{w}\| \xi(h) \rho(h, \mathbf{w})}{\delta_e(h)}$, such that $\alpha d_{\mathcal{G}}(i, j) \leq |y_i - y_j| \leq \beta d_{\mathcal{G}}(i, j)$.

Proof. For any two nodes i, j where $i \neq j$ we have:

$$\frac{|y_i - y_j|}{d_{\mathcal{G}}(i, j)} = \frac{|y_i - y_j|}{d_{\mathcal{M}}(h(\mathbf{x}_i), h(\mathbf{x}_j))} \frac{d_{\mathcal{M}}(h(\mathbf{x}_i), h(\mathbf{x}_j))}{d_{\mathcal{G}}(i, j)}. \quad (23)$$

By definition of the expansion factor of the embedding distortion (Eq. 3), we have that:

$$\frac{d_{\mathcal{M}}(h(\mathbf{x}_i), h(\mathbf{x}_j))}{d_{\mathcal{G}}(i, j)} \leq \delta_e(h). \quad (24)$$

Furthermore:

$$\frac{|y_i - y_j|}{d_{\mathcal{M}}(h(\mathbf{x}_i), h(\mathbf{x}_j))} = \frac{|\langle \mathbf{w}, h(\mathbf{x}_i) - h(\mathbf{x}_j) \rangle|}{d_{\mathcal{M}}(h(\mathbf{x}_i), h(\mathbf{x}_j))} \leq \frac{\|\mathbf{w}\| \|h(\mathbf{x}_i) - h(\mathbf{x}_j)\|}{d_{\mathcal{M}}(h(\mathbf{x}_i), h(\mathbf{x}_j))} \leq \|\mathbf{w}\| \zeta(h), \quad (25)$$

where the first inequality is due to Cauchy-Schwarz.

Putting together all of the above we get the upper bound:

$$\frac{|y_i - y_j|}{d_{\mathcal{G}}(i, j)} \leq \|\mathbf{w}\| \zeta(h) \delta_e(h). \quad (26)$$

Following a similar line of reasoning we can write:

$$\frac{|y_i - y_j|}{d_{\mathcal{G}}(i, j)} = \frac{|y_i - y_j|}{d_{\mathcal{M}}(h(\mathbf{x}_i), h(\mathbf{x}_j))} \frac{d_{\mathcal{M}}(h(\mathbf{x}_i), h(\mathbf{x}_j))}{d_{\mathcal{G}}(i, j)} \geq \frac{|y_i - y_j|}{d_{\mathcal{M}}(h(\mathbf{x}_i), h(\mathbf{x}_j))} \frac{1}{\delta_c(h)}. \quad (27)$$

By definition of the Euclidean inner product we have:

$$|y_i - y_j| = |\langle w, h(\mathbf{x}_i) - h(\mathbf{x}_j) \rangle| = \|\mathbf{w}\| \|h(\mathbf{x}_i) - h(\mathbf{x}_j)\| |\cos(\theta_{ij})| \quad (28)$$

where $\theta_{ij} = \angle(w, h(\mathbf{x}_i) - h(\mathbf{x}_j))$ and as such $\rho(h, \mathbf{w}) = \min_{\substack{i,j \in \mathcal{V} \\ i \neq j}} |\cos(\theta_{ij})|$. Knowing this we can write:

$$\frac{|\langle w, h(\mathbf{x}_i) - h(\mathbf{x}_j) \rangle|}{d_{\mathcal{M}}(h(\mathbf{x}_i), h(\mathbf{x}_j))} = \frac{\|\mathbf{w}\| \|h(\mathbf{x}_i) - h(\mathbf{x}_j)\| |\cos(\theta_{ij})|}{d_{\mathcal{M}}(h(\mathbf{x}_i), h(\mathbf{x}_j))} \geq \|\mathbf{w}\| \xi(h) \rho(h, \mathbf{w}), \quad (29)$$

such that we can conclude:

$$\frac{|y_i - y_j|}{d_{\mathcal{G}}(i, j)} \geq \frac{\|\mathbf{w}\| \xi(h) \rho(h, \mathbf{w})}{\delta_c(h)} \quad (30)$$

and in succession:

$$\frac{\|\mathbf{w}\| \xi(h) \rho(h, \mathbf{w})}{\delta_c(h)} d_{\mathcal{G}}(i, j) \leq |y_i - y_j| \leq \|\mathbf{w}\| \zeta(h) \delta_e(h) d_{\mathcal{G}}(i, j), \quad (31)$$

which completes the proof. \square

Proposition 4.3 Let \mathcal{G} be the input graph, f be the model, h the embedding function, and g the solver function, all as defined in Thm. 4.1. Furthermore, let h be an embedding of the graph into Euclidean space \mathbb{R}^d . The model distortion of f is

$$k(f) = \frac{\delta(h)}{\rho(h, \mathbf{w})}. \quad (32)$$

Proof. Given that h maps into the ambient Euclidean space, we immediately get that $\xi(h) = \zeta(h) = 1$ and from the definition of model distortion we obtain

$$k(f) = \frac{\delta(h)}{\rho(h, \mathbf{w})}. \quad (33)$$

\square

Proposition 4.4 Let \mathcal{G} be the input graph, f be the model, h the embedding function, and g the solver function, all as defined in Thm. 4.1. If $\delta(h) = 1$, the model distortion of f is

$$k(f) = \frac{\zeta(h)}{\xi(h) \rho(h, \mathbf{w})}. \quad (34)$$

Proof. This result is a direct consequence of the fact that the embedding has no distortion due to it being a similarity/isometry, which implies that $\delta(h) = \delta_c(h) \delta_e(h) = 1$, and from the definition of model distortion we obtain

$$k(f) = \frac{\zeta(h)}{\xi(h) \rho(h, \mathbf{w})}. \quad (35)$$

\square

We will now present two Lemmas that hold more general value, which will be used in the proof of Prop. 4.5.

Lemma C.1 (Submanifolds with induced Euclidean metric). *Let \mathcal{G} be the input graph, f be the model, h the embedding function, and g the solver function, all as defined in Thm. 4.1. Furthermore, let h be an embedding of the graph into a Riemannian submanifold of with the induced geodesic distance, i.e., $h : (\mathcal{G}, d_{\mathcal{G}}) \rightarrow (\mathcal{M}, d_{\mathcal{M}})$ and*

$$d_{\mathcal{M}}(a, b) = \inf_{\gamma} \int_0^1 \|\gamma'(t)\| dt,$$

such that $\gamma(0) = a, \gamma(1) = b$. Then model distortion of f is $k(f) = \frac{\delta(h)}{\xi(h) \rho(h, \mathbf{w})}$.

Proof. Note that under the induced metric, the length functional of a curve on the manifold $\gamma : [0, 1] \rightarrow \mathcal{M}$ with endpoints $\gamma(0) = h(\mathbf{x}_i), \gamma(1) = h(\mathbf{x}_j)$ satisfies:

$$L(\gamma) = \int_0^1 \|\gamma'(t)\| dt \geq \left\| \int_0^1 \gamma'(t) dt \right\| = \|\gamma(1) - \gamma(0)\| = \|h(\mathbf{x}_i) - h(\mathbf{x}_j)\|, \quad (36)$$

due to the triangle inequality and the fundamental theorem of calculus. The geodesic distance, represented as the minimal possible length of any curve satisfying the length functional, must also respect the above inequality, which implies that:

$$\zeta(h) = \max_{\substack{i, j \in \mathcal{V} \\ i \neq j}} \frac{\|h(\mathbf{x}_i) - h(\mathbf{x}_j)\|}{d_{\mathcal{M}}(h(\mathbf{x}_i), h(\mathbf{x}_j))} \leq 1. \quad (37)$$

We can now redefine the upper constant in Thm. 4.1 to $\beta = \|\mathbf{w}\| \delta_e(h)$. The model distortion then becomes

$$k(f) = \frac{\beta}{\alpha} = \frac{\|\mathbf{w}\| \delta_e(h)}{\frac{\|\mathbf{w}\| \xi(h) \rho(h, \mathbf{w})}{\delta_c(h)}} = \frac{\delta(h)}{\xi(h) \rho(h, \mathbf{w})}. \quad (38)$$

□

Lemma C.2 (Submanifolds with conformal metric). *Let \mathcal{G} be the input graph, f be the model, h the embedding function, and g the solver function, all as defined in Thm. 4.1. Furthermore, let h be an embedding of the graph into a Riemannian submanifold equipped with a conformal metric, i.e., $h : (\mathcal{G}, d_{\mathcal{G}}) \rightarrow (\mathcal{M}, d_{\mathcal{M}})$ where \mathcal{M} has metric $g : T_x \mathcal{M} \times T_x \mathcal{M} \rightarrow \mathbb{R}$ such that for two tangent vectors $\mathbf{v}, \mathbf{w} \in T_x \mathcal{M}$, $g_x(\mathbf{v}, \mathbf{w}) = \lambda(p)^2 \langle \mathbf{v}, \mathbf{w} \rangle$. Assume that the conformal factor λ is uniformly bounded such that $0 < \lambda_{\min} \leq \lambda \leq \lambda_{\max}$. Define the quantity*

$$\xi^{\mathcal{M}^{\mathbb{E}}}(h) = \min_{i, j \in \mathcal{V}, i \neq j} \frac{\|h(\mathbf{x}_i) - h(\mathbf{x}_j)\|}{d_{\mathcal{M}^{\mathbb{E}}}(h(\mathbf{x}_i), h(\mathbf{x}_j))}, \quad (39)$$

where $d_{\mathcal{M}^{\mathbb{E}}}(\cdot, \cdot)$ is the geodesic distance under the induced metric. Then, the model distortion of f is

$$k(f) = \frac{\lambda_{\max} \delta(h)}{\lambda_{\min} \xi^{\mathcal{M}^{\mathbb{E}}}(h) \rho(h, \mathbf{w})}. \quad (40)$$

Proof. The length functional of a curve $\gamma : [0, 1] \rightarrow \mathcal{M}$ with endpoints $\gamma(0) = h(\mathbf{x}_i), \gamma(1) = h(\mathbf{x}_j)$, on a manifold with metric g is defined as:

$$L_g(\gamma) = \int_0^1 \sqrt{g_{\gamma(t)}(\gamma'(t), \gamma'(t))} dt. \quad (41)$$

When the metric takes the conformal form described above, it reads as:

$$L_g(\gamma) = \int_0^1 \lambda(\gamma(t)) \|\gamma'(t)\| dt, \quad (42)$$

which indeed confirms that distances under a conformal metric are (appropriately) scaled counterparts of the distances under the induced Euclidean metric (remember that conformal in this scenario means that angles are preserved, while distances are scaled). Given that the conformal factor is positive, using the bound $\lambda_{\min} \leq \lambda \leq \lambda_{\max}$ pointwise gives

$$\lambda_{\min} L_{g^{\mathbb{E}}}(\gamma) \leq L_g(\gamma) \leq \lambda_{\max} L_{g^{\mathbb{E}}}(\gamma), \quad (43)$$

where $L_{g^{\mathbb{E}}}$ is the length functional for a submanifold with the induced Euclidean metric, as described in the proof of Prop. C.1. The geodesic distance is the one corresponding to the curve that minimizes the length function, and thus taking the infimum over curves will respect monotonicity such that we can arrive at:

$$\lambda_{\min} d_{\mathcal{M}^{\mathbb{E}}}(h(\mathbf{x}_i), h(\mathbf{x}_j)) \leq d_{\mathcal{M}}(h(\mathbf{x}_i), h(\mathbf{x}_j)) \leq \lambda_{\max} d_{\mathcal{M}^{\mathbb{E}}}(h(\mathbf{x}_i), h(\mathbf{x}_j)), \quad (44)$$

where $d_{\mathcal{M}^{\mathbb{E}}}(\cdot, \cdot)$ denotes the distance under the induced Euclidean metric. We can then write:

$$\zeta(h) = \max_{\substack{i,j \in \mathcal{V} \\ i \neq j}} \frac{\|h(\mathbf{x}_i) - h(\mathbf{x}_j)\|}{d_{\mathcal{M}}(h(\mathbf{x}_i), h(\mathbf{x}_j))} \leq \max_{\substack{i,j \in \mathcal{V} \\ i \neq j}} \frac{\|h(\mathbf{x}_i) - h(\mathbf{x}_j)\|}{\lambda_{\min} d_{\mathcal{M}^{\mathbb{E}}}(h(\mathbf{x}_i), h(\mathbf{x}_j))} \leq \frac{1}{\lambda_{\min}}, \quad (45)$$

$$\xi(h) = \min_{\substack{i,j \in \mathcal{V} \\ i \neq j}} \frac{\|h(\mathbf{x}_i) - h(\mathbf{x}_j)\|}{d_{\mathcal{M}}(h(\mathbf{x}_i), h(\mathbf{x}_j))} \geq \min_{\substack{i,j \in \mathcal{V} \\ i \neq j}} \frac{\|h(\mathbf{x}_i) - h(\mathbf{x}_j)\|}{\lambda_{\max} d_{\mathcal{M}^{\mathbb{E}}}(h(\mathbf{x}_i), h(\mathbf{x}_j))} \geq \frac{1}{\lambda_{\max}} \xi^{\mathcal{M}^{\mathbb{E}}}(h). \quad (46)$$

Using all this information, we can rewrite the bi-Lipschitz bounds of the model distortion according to Thm. 4.1, by redefining both the upper and lower constants

$$k(f) = \frac{\|\mathbf{w}\| \delta_e(h)}{\frac{\lambda_{\min}}{\|\mathbf{w}\| \xi^{\mathcal{M}^{\mathbb{E}}}(h) \rho(h, \mathbf{w})}} = \frac{\lambda_{\max} \delta(h)}{\lambda_{\min} \xi^{\mathcal{M}^{\mathbb{E}}}(h) \rho(h, \mathbf{w})}. \quad (47)$$

Unsurprisingly, the result is similar to the case for submanifolds with induced metric in Prop. C.1, but rescaled based on the conformal bounds. \square

Proposition 4.5 Let \mathcal{G} be the input graph, f be the model, h the embedding function, and g the solver function, all as defined in Thm. 4.1. Let h be an embedding function that embeds the Poincaré ball \mathcal{B}_1^d and define $\eta := \max_{i \in \mathcal{V}} \|h(\mathbf{x}_i)\|$. Then, the model distortion of f is

$$k(f) = \frac{\delta(h)}{(1 - \eta^2) \rho(h, \mathbf{w})}. \quad (48)$$

Proof. We start by noting that, given the domain of definition of \mathcal{B}_1^d we have:

$$\lambda_{\min} = \lim_{\|p\| \rightarrow 0} \lambda(p) = \lim_{\|p\| \rightarrow 0} \frac{2}{1 - \|p\|^2} = 2. \quad (49)$$

We now proceed by making a direct comparison of the difference in the length of a chord connecting any two points within the ball and its length under the manifold metric. Given the convexity of the domain, we can write any chord connecting points $h(\mathbf{x}_i)$ and $h(\mathbf{x}_j)$ as a convex combination:

$$\gamma(t) = t h(\mathbf{x}_i) + (1 - t) h(\mathbf{x}_j), \quad (50)$$

for $t \in (0, 1)$. We can then deduce the following two facts:

$$\|\gamma(t)\| \leq \|t h(\mathbf{x}_i)\| + \|(1 - t) h(\mathbf{x}_j)\| \leq \max\{\|h(\mathbf{x}_i)\|, \|h(\mathbf{x}_j)\|\} \quad (51)$$

$$\|\gamma'(t)\| = \|h(\mathbf{x}_i) - h(\mathbf{x}_j)\|, \quad (52)$$

where in the first equation we use the triangle inequality and the second implies a constant speed. Letting $c_{ij} = \max\{\|h(\mathbf{x}_i)\|, \|h(\mathbf{x}_j)\|\}$, the first inequality above implies that $1 - \|\gamma(t)\|^2 \geq 1 - c_{ij}^2$ and therefore we obtain:

$$\frac{2}{1 - \|\gamma(t)\|^2} \leq \frac{2}{1 - c_{ij}^2} \quad (53)$$

We can now use the fact that $\eta = \max_i \|h(\mathbf{x}_i)\|$ and the formula for the length functional under the conformal metric, as presented in the Lemma Prop. C.2, such that:

$$L_{\mathbf{g}}(\gamma) = \int_0^1 \lambda(\gamma(t)) \|\gamma'(t)\| dt \leq \int_0^1 \frac{2\|h(\mathbf{x}_i) - h(\mathbf{x}_j)\|}{1 - c_{ij}^2} dt = \frac{2\|h(\mathbf{x}_i) - h(\mathbf{x}_j)\|}{1 - c_{ij}^2} \leq \frac{2\|h(\mathbf{x}_i) - h(\mathbf{x}_j)\|}{1 - \eta^2}. \quad (54)$$

One the other hand, for any chord, we have that:

$$L_{\mathbf{g}}(\gamma) = \int_0^1 \lambda(\gamma(t)) \|\gamma'(t)\| dt \geq \int_0^1 \lambda_{\min} \|\gamma'(t)\| dt = 2\|h(\mathbf{x}_i) - h(\mathbf{x}_j)\|. \quad (55)$$

Given all chords within the ball have constant speed, we get:

$$2 \|h(\mathbf{x}_i) - h(\mathbf{x}_j)\| \leq d_B(h(\mathbf{x}_i), h(\mathbf{x}_j)) \leq \frac{2}{1 - \eta^2} \|h(\mathbf{x}_i) - h(\mathbf{x}_j)\|. \quad (56)$$

Using the notation of Thm. 4.1, the above result translates to $\zeta(h) \leq \frac{1}{2}$ and $\xi(h) \geq \frac{1-\eta^2}{2}$, which in turn implies that we can redefine the upper and lower constants as $\beta = \frac{1}{2} \|\mathbf{w}\| \delta_e(h)$ and $\alpha = \frac{(1-\eta^2) \|\mathbf{w}\| \rho(h, \mathbf{w})}{2 \delta_e(h)}$. By the definition of model distortion we obtain:

$$k(f) = \frac{\beta}{\alpha} = \frac{\delta(h)}{(1 - \eta^2) \rho(h, \mathbf{w})}. \quad (57)$$

We conclude by noting that the final result is essentially identical for a given curvature magnitude c , as this factor is directly absorbed inside the quantity η (by def. of the Poincaré ball) such that the model distortion becomes $k(f) = \frac{\delta(h)}{(1 - c\eta^2) \rho(h, \mathbf{w})}$. \square

D. Gromov δ -hyperbolicity

We recall the definition of δ -Gromov hyperbolicity based on the four-point condition, originally introduced by Gromov as a purely metric characterization of negative curvature (Gromov, 1987; Bonk & Schramm, 2011). Trees are prototypical examples of hyperbolic metric spaces. Accordingly, the four-point condition quantifies the extent to which a metric space exhibits tree-like behavior.

Definition D.1 (Gromov hyperbolicity via the four-point condition). A metric space (M, d) is said to be δ -hyperbolic, if for some $\delta > 0$, it satisfies the *four-point condition*: for any $x, y, z, t \in M$, define

$$S_1 = d(x, y) + d(z, t), \quad S_2 = d(x, z) + d(y, t), \quad S_3 = d(x, t) + d(y, z).$$

Then the two largest values among $\{S_1, S_2, S_3\}$ differ by at most 2δ . The *Gromov hyperbolicity constant* δ^* of (M, d) is the smallest $\delta^* > 0$ such that (M, d) is δ^* -hyperbolic.

This formulation is particularly appealing from a computational perspective, as the hyperbolicity of a finite metric space can be evaluated directly by checking the four-point condition over all quadruples of points.

Real-world datasets. We recomputed Gromov δ -hyperbolicity for all datasets used, using an exact algorithm from the SageMath library (Stein & Joyner, 2005) (BCCM). This is different from previous papers that only provided results from an approximate algorithm, that approximates δ by sampling quadruples of nodes. For that reason there are some differences in the values reported. In particular Chami et al. (2019) reported $\delta = 1$ for Airport, $\delta = 3.5$ for PubMed and $\delta = 11$ for Cora using the approximate algorithm, while the exact algorithm yields $\delta = 2$ for Airport, $\delta = 4.5$ for PubMed and $\delta = 4$ for Cora.

Because of the importance of Gromov δ -hyperbolicity as a decision criterion in the context of HGNNs, we recomputed it for many well-known real-world datasets, which can be reviewed in Table 3. Again, all values are computed using SageMath (Stein & Joyner, 2005) (BCCM algorithm) on the largest connected components. In case of multiple components, the smaller components achieved a smaller or equal delta (e.g. on Cora and Airport). Most real-world dataset exhibit small delta values, with the exception of Minesweeper which is a synthetic dataset on a 50×50 grid graph. Exact computation for larger graphs, like for example OGBN graphs (Hu et al., 2020), is usually infeasible with an exact algorithm and in particular impossible in SageMath due to the limit of 65536 nodes and memory limitations. In these cases sampling-based methods are the only option and therefore no results are reported here. We would like to note however that computing or even only finding approximations to δ -hyperbolicity on large graphs is a research topic in discrete mathematics on its own (Cohen et al., 2012; Coudert et al., 2022).

Table 3. Exact δ -hyperbolicity values of many well-known real-world datasets. Values are computed using SageMath (Stein & Joyner, 2005) (BCCM algorithm) on the largest connected components. In case of multiple components, the smaller components achieved a smaller or equal delta (e.g. on Cora and Airport). On PPI all subgraphs achieved the same $\delta = 2$. Most real-world dataset exhibit small delta values, with the exception of Minesweeper which is a synthetic dataset on a 50×50 grid graph.

Category	Dataset	δ
Planetoid Citation Graphs (Sen et al., 2008)	Cora	4.0
	Citeseer	6.5
	Pubmed	4.5
Hyperbolic GNN Benchmarks (Chami et al., 2019; Greene et al., 2015)	Disease	0.0
	Airport	2.0
	PPI	2.0
Small-scale Social Networks (Rozemberczki & Sarkar, 2020)	Facebook Page-Page	4.0
	LastFM Asia	3.5
Heterophilous Node Classification Benchmarks (Platonov et al., 2023)	Roman-Empire	3.5
	Amazon-Ratings	11.0
	Minesweeper	49.0
	Questions	3.5
	Tolokers	2.5
Product Co-purchase Graphs (McAuley et al., 2015)	Amazon Computers	2.5
	Amazon Photo	3.0
Wikipedia Networks (Rozemberczki et al., 2021)	Chameleon	2.5
	Squirrel	2.5
Actor Co-occurrence Network (Tang et al., 2009)	Actor	3.0
	USA	1.5
Air Transportation Networks (Ribeiro et al., 2017)	Brazil	1.0
	Europe	1.0
	Cornell	2.0
University Web Pages (WebKB) (Pei et al., 2020)	Texas	1.5
	Wisconsin	2.0
	Coauthor-CS	4.0
Co-authorship Networks (Shchur et al., 2018)	Coauthor-Physics	4.0

E. Experimental Setup

Here, we summarize the evaluation protocol for each task and synthetic or real-world dataset.

E.1. Tasks and Real-world Datasets

Tasks On synthetic datasets, we consider all four tasks: (i) **Pairwise Distance Prediction (PDP)**, where the goal is to regress the shortest-path distance between pairs of nodes; (ii) **Node Regression**, where node-level continuous targets (distance to anchor node) are predicted; (iii) **Node Classification**, where node-level discrete targets (distance to anchor node as a class) are predicted; and (iv) **Link Prediction**, formulated as a binary classification task.

For LP tasks, in all experiments, we randomly split edges into 85/5/10% for training, validation and test set, respectively. Negative edges are sampled uniformly using PyG’s negative edge sampling utility. We would also like to note that even though most prior work used a distance-based decoder, there are other other valid choices, like an MLP on top of the concatenated embeddings. Since the goal of this work is to asses the effect of geometric inductive biases, we chose this decoder to isolate the effect of geometry as good as we can. Analyzing other decoders, both theoretically and empirically, is another interesting direction for future work.

For the real-world datasets, we use well-established benchmarks from the hyperbolic GNN literature, including Disease, Airport, Cora, Pubmed, and Citeseer, which exhibit varying levels of δ -hyperbolicity. On these datasets, we focus on **Link Prediction (LP)** and **Node Classification (NC)** tasks, following standard dataset splits and evaluation protocols used in prior work. For NC, we use a corrected 70/15/15% split for both Airport and Disease, and standard splits (Kipf & Welling, 2017) with 20 train examples per class, 500 overall for validation and the rest as test set for Cora, PubMed and Citeseer.

For each dataset, we generate 10 independent data splits on which we perform the experimental runs. Each splits also has a different random seed for initializing all random operations (like weight initialization). All reported results are averaged over these 10 splits, and means and standard deviations are reported.

Disease NC data split bug. There was a bug in the original data splitting function on Disease that resulted in a 71.6/4/24.3% split instead of the reported 30/10/60%. Additionally the dataset is very unbalanced (of the overall nodes 20% are label 1 and 80% are label 0), but using the original splitting function this was not reflected on the train set, because the test and validation sets had a fixed 50%/50% ratio of the two labels. This led to even less training samples of the minority class, changing the training dynamics significantly compared to all other NC experiments. In our experiments we refer to the corrected version by Disease*, where we split the nodes using a standard 70/15/15% split, keeping the ratio of the two classes the same in all splits. For full transparency we also report the results using the original splitting ratio with a slightly adapted 70/5/25% splitting (compared to the original 71.6/4/24.3% split) in Appendix F.4.

Airport data leakage. The use of the same splitting function that was used on Disease on the Airport dataset, resulted in data leakage as it was built for binary classification. Applying it to the 4-class classification of the Airport dataset resulted in leakage of validation and test labels to the train set. We fixed this problem by using PyG’s standard random node splitting function and only report the results on the corrected splits.

E.2. Synthetic Datasets

For the **PDP task**, we use two synthetic graphs: a tree graph and a grid graph. For each split, node pairs are randomly partitioned using a 70/15/15% split. In both cases, the nodes are equipped with 100-dimensional random (Gaussian) and sparse (10%) features. We chose these features for all our synthetic tasks, to isolate the effect of geometry, but to be still close to real-world features that are often high-dimensional but sparse.

For **Node Regression** and **Node Classification**, we use a synthetic tree with depth $h = 4$ and a varying branching factor of $b = 100, 2, 2, 2$. This means after root the tree has four levels, with increasing number of nodes: 100, 200, 400, 800. The motivation for this was to work in a tree setting that is not extremely unbalanced w.r.t. to the numbers of nodes per level. The nodes are equipped with 100-dimensional random (Gaussian) and sparse (10%) features. For regression, the anchor node is set as the root, therefore the label is the distance to the root node (values 1 to 4). For classification these four values are the four classes. In both cases we use splits with 20 train examples per class, 500 overall for validation and the rest as test set as for Cora etc. Since only HGNN is not perfectly reproducible for NR with $d = 3$, we additionally run the experiments on the usual 10 splits, ten times and report the average over these in order to be as close as possible to full reproducibility.

For **Link Prediction**, we use the $Tree1111_\gamma$ synthetic dataset introduced in (Katsman & Gilbert, 2025) with the standard 85/5/10%. In this dataset, the graph is a branching factor 10 tree with height 4 and the features are generated procedurally, level-by-level starting from $x^{(0)} \sim \mathcal{N}(0, I_{1000})$ and then $x^{(n)} = \gamma \cdot \text{parent}(x^{(n)}) + \nu$, where $\nu \sim \mathcal{N}(0, I_{1000})$. Now, when $\gamma = 0$, node features are i.i.d. samples from the base distribution and contain no graph information; therefore, any nontrivial performance must come from the model’s ability to exploit the graph. As γ increases, features progressively “leak” structural information. In this sense, it provides a controlled setting to evaluate whether and to what extent the graph structure itself is actually necessary to solve the task. Katsman & Gilbert (2025) already showed results for the MLP on a range of γ -values between 0 and 1.0 and some advantage of using HyboNet for $\gamma = 0$. We provide results over all values of γ using all our GNN models and the MLP.

Additionally, as described in the main text, we experiment with versions of Disease and Airport, where we corrupt the features by Gaussian noise of varying standard deviation.

E.3. Models

Our experimental comparison includes:

- **HGNNs**, operating either fully in hyperbolic space, such as HyboNet (Chen et al., 2022), or using tangent-space-based methods, such as HGNN (Chami et al., 2019);
- **Euclidean GNNs**, operating in standard Euclidean space, including GCN (Kipf & Welling, 2017), GAT (Veličković et al., 2018), and a Euclidean variant of HyboNet (Chen et al., 2022) that we denote by HyboNet (Eucl.);
- **MLP** that does not consider the graph structure and thus operates solely on the node features (using Euclidean Neural Network operations).

For hyperbolic models, node features are first mapped from Euclidean space to hyperbolic space using the exponential

map at the origin. All subsequent message-passing and prediction operations are performed within the chosen hyperbolic manifold. Euclidean counterparts follow identical architectural choices where applicable, differing only in the underlying geometry.

E.4. Training and Hyperparameter Tuning

Hyperparameters are selected based on validation performance. For each model and task, we tune the learning rate, activation function, number of layers, embedding dimension, weight decay, and dropout using a mixture of random and grid search. For NC we additionally tune the loss function (Margin or CE), and for both LP and NC, the normalization of the training adjacency and the use of gradient clipping. The exceptions are the noisy Disease and Airport experiments, and the curvature experiments for HGCN on NR. For the noisy Disease and Airport experiments, we tuned all models only for a noise level of 0.5 and the HGNC uses the same hyperparameters as HGNC on NR (except for the curvature). For hyperbolic models, optimization is performed using the Riemannian Adam optimizer (Becigneul & Ganea, 2019), while Euclidean models are trained using the standard Adam optimizer (Kingma & Ba, 2015).

As is standard in the literature, we use a minimum number of epochs of 100, a maximum of 5000 and early stopping if the validation criterion did not improve over 500 epochs. When applicable, we also tune the use of attention mechanisms. All reported results correspond to the hyperparameter configuration that achieves the best performance on the validation set. The experiments on were performed using Nvidia A100 and Nvidia H100 GPUs.

Hyperparameter configuration for all experiments can be found in the code repository.

F. Additional Results

F.1. Pairwise Distance Prediction Task

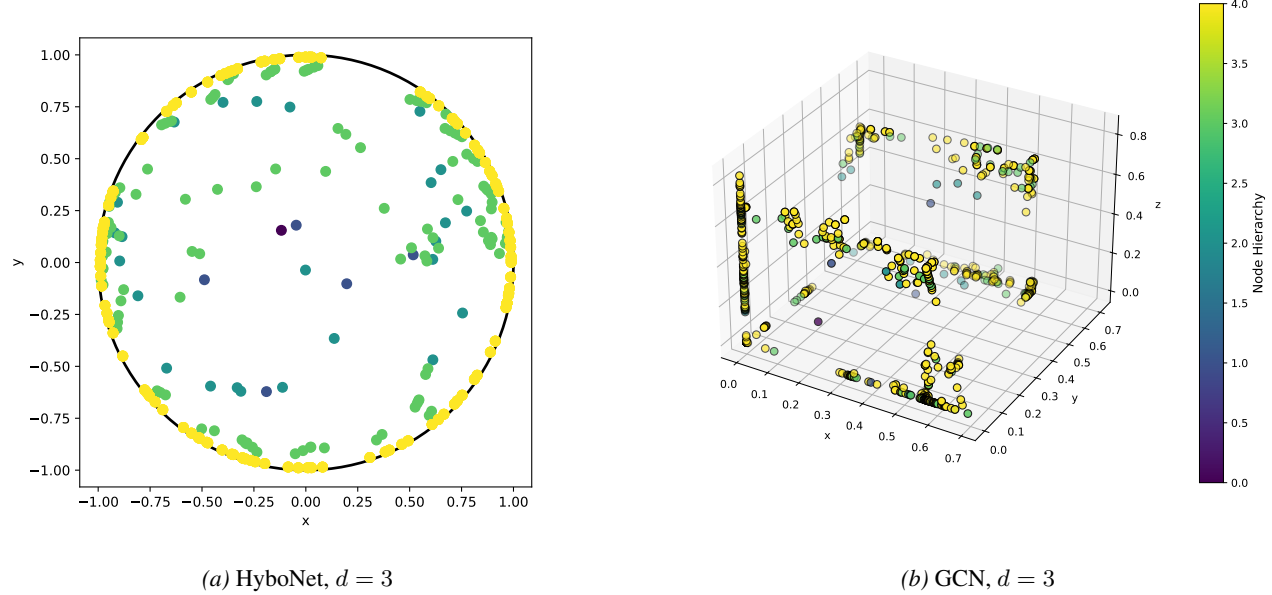


Figure 6. Visualization of the embedding spaces learned by HyboNet and GCN models for $d = 3$ for the PDP task on the *tree*.

We report the results of the Pairwise Distance Prediction (PDP) task in Tables 4 and 5, evaluated across varying embedding dimensions on both the *tree* and *grid* graphs, and corresponding to Fig. 2. Figure 6 shows the learned embeddings of HyboNet and GCN for the *tree* graph with embedding dimension $d = 3$. For HyboNet, the points form 3d Lorentz space are mapped to the Poincaré disc. Here, node embeddings of close to the root nodes are located closer to the center and further away from the root and leaf nodes positioned toward the boundary, reflecting the underlying hierarchical structure of the graph. In contrast, GCN embeddings tend to occupy a roughly cubic region of the Euclidean space, suggesting an increased

geometric distortion of pairwise distances.

As a sanity check, we conduct a *control experiment* in which the target pairwise distances are randomly permuted. This experiment assesses whether the observed performance differences persist in the absence of meaningful geometric signal, thereby helping to disentangle the contribution of geometric inductive bias from architectural effects. The results of the null experiment are reported in Table 6.

The PDP results can also be viewed from another, more qualitative perspective by explicitly confronting pairwise distances in data versus embedding space. To do this we plot the averaged pairwise distances (and the standard deviation) in embedding space conditioned on the true pairwise graph distances. Then we perform a linear fit on these points in the plot and report the R^2 score. The R^2 score or the coefficient of determination, measures how much of the variation in the dependent variable (average pairwise distance in embeddings space) is explained by the linear model (which is the true underlying relation here). An R^2 close to 1 means the points lie close to the fitted line, while an R^2 near 0 means the line explains little of the data's variability. So for us, it measures how faithfully the embedding preserves the graph metric on average. Results comparing HyboNet and Euclidean HyboNet are reported in Fig. 7. At low embedding dimension, HyboNet achieves the highest R^2 on the *tree* graph (Table 7). As the embedding dimension increases, the performance gap progressively narrows and eventually vanishes.

Overall, these results show that when supervision explicitly depends on pairwise distances, message passing can exploit the geometric inductive bias of the latent space to recover low-distortion structure, especially in low-dimensional regimes where representational capacity is limited.

Table 4. Stress loss (\downarrow) (mean \pm std) across embedding dimensionality for the pairwise-distance prediction task on the synthetic tree graph.

MODEL	3	8	16	32	64	128
GCN	0.0678 \pm 0.0035	0.0355 \pm 0.0012	0.0194 \pm 0.0015	0.0127 \pm 0.0005	0.0081 \pm 0.0002	0.0037 \pm 0.0002
GAT	0.0464 \pm 0.0018	0.0183 \pm 0.0004	0.0106 \pm 0.0004	0.0070 \pm 0.0004	0.0047 \pm 0.0003	0.0036 \pm 0.0003
HYBONET (EUCL.)	0.0464 \pm 0.0013	0.0227 \pm 0.0041	0.0158 \pm 0.0007	0.0094 \pm 0.0006	0.0083 \pm 0.0003	0.0091 \pm 0.0016
HYBONET	0.0383 \pm 0.0051	0.0058 \pm 0.0007	0.0035 \pm 0.0001	0.0034 \pm 0.0002	0.0034 \pm 0.0002	0.0035 \pm 0.0001
HGCN	0.0542 \pm 0.0054	0.0092 \pm 0.0006	0.0055 \pm 0.0003	0.0021 \pm 0.0004	0.0007 \pm 0.0001	0.0006 \pm 0.0001

Table 5. Stress loss (\downarrow) (mean \pm std) across embedding dimensionality for the pairwise-distance prediction task on the synthetic grid graph.

MODEL	3	8	16	32	64	128
GCN	0.0263 \pm 0.0020	0.0128 \pm 0.0002	0.0119 \pm 0.0001	0.0116 \pm 0.0002	0.0106 \pm 0.0002	0.0102 \pm 0.0001
GAT	0.0235 \pm 0.0031	0.0132 \pm 0.0006	0.0120 \pm 0.0010	0.0116 \pm 0.0005	0.0114 \pm 0.0003	0.0112 \pm 0.0002
HYBONET (EUCL.)	0.1258 \pm 0.0664	0.0206 \pm 0.0013	0.0152 \pm 0.0004	0.0131 \pm 0.0001	0.0122 \pm 0.0002	0.0113 \pm 0.0002
HYBONET	0.1792 \pm 0.0532	0.0274 \pm 0.0048	0.0184 \pm 0.0008	0.0180 \pm 0.0026	0.0186 \pm 0.0017	0.0181 \pm 0.0030
HGCN	0.1834 \pm 0.0283	0.0236 \pm 0.0120	0.0124 \pm 0.0004	0.0115 \pm 0.0001	0.0112 \pm 0.0002	0.0112 \pm 0.0002

Table 6. Stress loss (\downarrow) (mean \pm std) for tree and grid graphs for the label-permutation control experiment, averaged over 10 random seeds.

MODEL	TREE		GRID	
	3	128	3	128
GCN	0.1515 \pm 0.0048	0.1528 \pm 0.0050	0.5349 \pm 0.0111	0.5796 \pm 0.0079
GAT	0.1515 \pm 0.0048	0.1515 \pm 0.0048	0.5784 \pm 0.0102	0.5687 \pm 0.0057
HYBONET (EUCL.)	0.1577 \pm 0.0053	0.1561 \pm 0.0086	0.5702 \pm 0.0066	0.5824 \pm 0.0077
HYBONET	0.1520 \pm 0.0048	0.1564 \pm 0.0054	0.5767 \pm 0.0077	0.5713 \pm 0.0076
HGCN	0.1522 \pm 0.0048	0.1525 \pm 0.0053	0.5700 \pm 0.0054	0.5772 \pm 0.0049

Table 7. R^2 score (\uparrow) of a linear fit to the embedding distances (averaged per true distance) at embedding dimensions 3 and 128, for tree and grid graphs, averaged over 10 random seeds.

MODEL	TREE		GRID	
	3	128	3	128
GCN	0.3260 ± 0.0491	0.9737 ± 0.0008	0.9324 ± 0.0026	0.9679 ± 0.0004
GAT	0.4625 ± 0.0033	0.9778 ± 0.0013	0.9404 ± 0.0060	0.9617 ± 0.0005
HYBONET (EUCL.)	0.5006 ± 0.0158	0.9341 ± 0.0022	0.5776 ± 0.2634	0.9664 ± 0.0004
HYBONET	0.5979 ± 0.0449	0.9882 ± 0.0007	0.5129 ± 0.1746	0.9365 ± 0.0074
HGCN	0.3595 ± 0.0527	0.9992 ± 0.0001	0.3896 ± 0.1331	0.9681 ± 0.0012

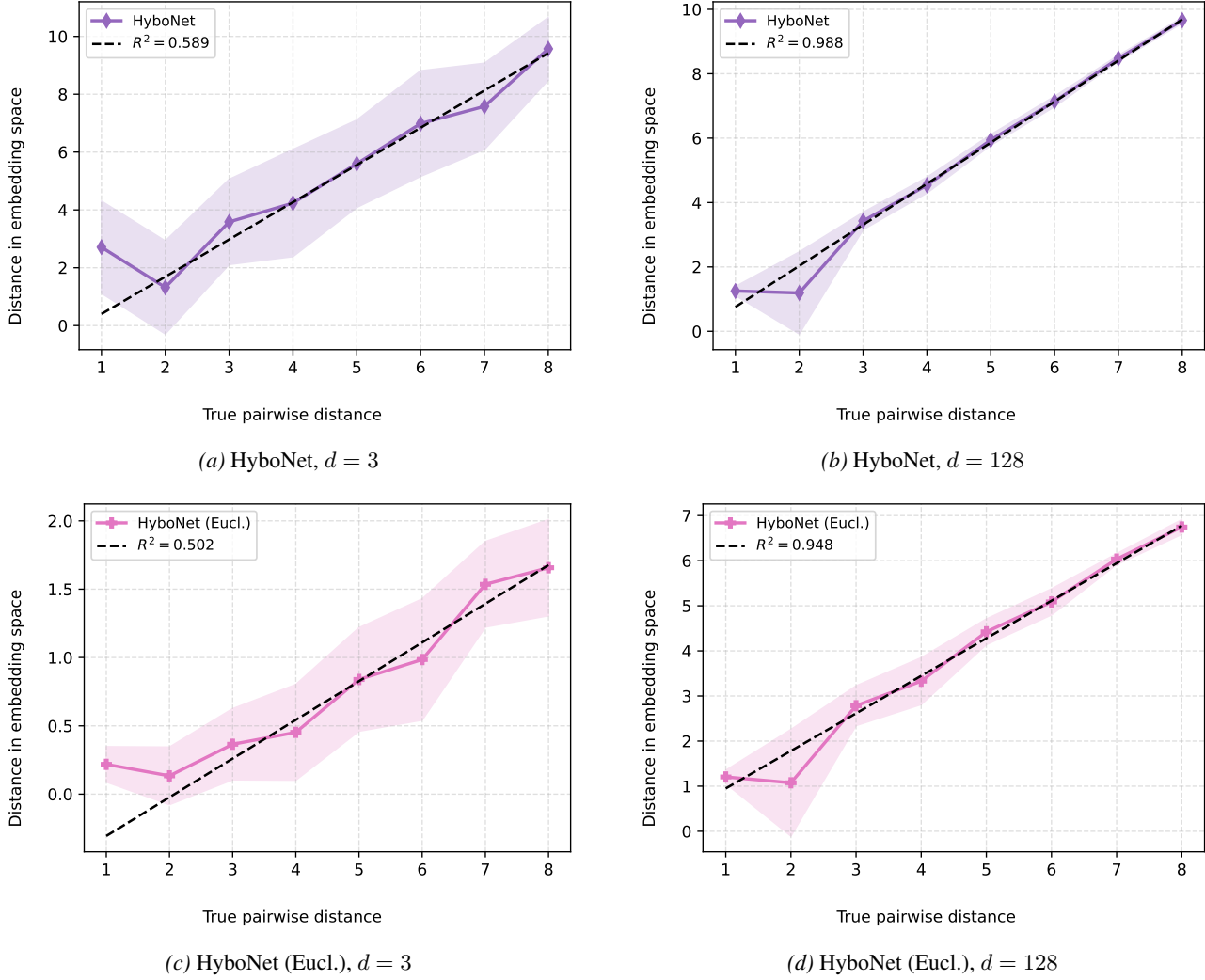


Figure 7. Line fit of the embedding distances plotted and averaged against the true graph distances for the pairwise-distance prediction task on the tree. Results are shown for HyboNet and HyboNet (Eucl.) graphs at low ($d = 3$) and high ($d = 128$) embedding dimensions. The R^2 score measures the goodness of fit of the line, i.e. how faithfully the embedding preserves graph distances.

F.2. Link Prediction

Real-world datasets. As mentioned in the main text, in addition to the Receiver Operator Characteristic Area under the Curve (ROC AUC) results, we also report average precision (AP) to give a more comprehensive picture. The full LP results on the real world datasets are in Table 8 for ROC AUC and Table 9 for AP. As for the PDP task, we also include HyboNet

Table 8. ROC AUC (\uparrow) results for real-world link prediction (LP). We report Gromov δ -hyperbolicity (lower is more hyperbolic).

MODEL	DISEASE $\delta = 0$	AIRPORT $\delta = 2$	CORA $\delta = 4$	PUBMED $\delta = 4.5$	CITESEER $\delta = 6.5$
MLP	98.43 \pm 0.74	97.66 \pm 0.12	90.33 \pm 0.94	94.52 \pm 0.26	91.45 \pm 0.68
GCN	91.67 \pm 1.79	96.58 \pm 0.35	92.98 \pm 1.01	95.03 \pm 0.19	96.02 \pm 0.50
GAT	93.25 \pm 1.59	95.67 \pm 0.33	93.50 \pm 0.68	96.77 \pm 0.18	93.32 \pm 0.92
HYBONET (EUCL.)	79.76 \pm 4.84	95.43 \pm 0.29	92.92 \pm 0.75	95.72 \pm 0.17	92.92 \pm 0.76
HYBONET	97.99 \pm 0.72	98.15 \pm 0.17	93.70 \pm 0.58	97.08 \pm 0.09	91.53 \pm 1.40
HGCN	95.16 \pm 2.50	97.66 \pm 0.15	93.88 \pm 1.09	96.86 \pm 0.11	94.46 \pm 0.61

 Table 9. AP (\uparrow) results for real-world link prediction (LP). We report Gromov δ -hyperbolicity (lower is more hyperbolic).

MODEL	DISEASE $\delta = 0$	AIRPORT $\delta = 2$	CORA $\delta = 4$	PUBMED $\delta = 4.5$	CITESEER $\delta = 6.5$
MLP	97.71 \pm 1.18	96.77 \pm 0.22	89.12 \pm 1.35	93.54 \pm 0.31	90.44 \pm 0.71
GCN	85.47 \pm 3.36	94.62 \pm 0.63	92.57 \pm 1.29	94.57 \pm 0.25	96.04 \pm 0.61
GAT	90.38 \pm 2.05	95.34 \pm 0.41	93.81 \pm 0.76	96.95 \pm 0.18	93.76 \pm 0.98
HYBONET (EUCL.)	75.03 \pm 6.59	94.52 \pm 0.47	92.78 \pm 0.88	95.79 \pm 0.13	93.80 \pm 0.74
HYBONET	96.54 \pm 1.62	97.55 \pm 0.38	93.78 \pm 0.66	97.01 \pm 0.09	92.47 \pm 1.44
HGCN	92.60 \pm 3.90	96.97 \pm 0.22	93.80 \pm 1.25	96.71 \pm 0.14	94.71 \pm 0.77

(Eucl.) as an additional comparison to isolate the effect of model architecture here. The AP results therefore do not offer a completely new perspective on the model’s performance, but merely underline the findings already made for ROC AUC. For full disclosure, we report the exact values of Stress Loss for the distortion analysis for LP. The absolute values are in Table 10 and the normalized values are in Table 11. We also report AP and absolute stress loss for the experiments on Disease and Airport, where the features are corrupted by noise in Figure 8.

Synthetic Datasets. We evaluate all our models on the $Tree1111_\gamma$ dataset from Katsman & Gilbert (2025), which varies node feature informativeness and enables probing model behavior across different feature–structure regimes. Similar to the noisy Disease and Airport experiments in real-world settings, these experiments further stress the role of geometry in a controlled synthetic setting. The results in Figure 9 reproduces the qualitative behavior of the real-world datasets across varying feature informativeness. All GNNs outperform the MLP for small values of γ as they can make use of structural information. All GNNs achieve smaller stress losses than the features and the MLP for small values of γ . GAT and HyboNet continue to do so for larger γ , while the MLP largely follows the trend of the features, which naturally achieve lower stress losses for higher γ values (features are more informative about the graph structure). The hyperbolic methods HGCN and HyboNet generally achieve better performance than GCN, but only HyboNet does so by achieving low stress losses. The notable exception here is GAT, which performs unusually strongly in this setting. We attribute this to the nearly orthogonal 1000-dimensional features used in $Tree1111_\gamma$, which act as near-unique node identifiers (similar to one-hot encodings); attention can leverage these signals while avoiding excessive smoothing, unlike degree-normalized aggregation as in GCN. Last, other than on the noisy real-world experiences, HGCN performs better than HyboNet, which we also attribute to the different attention mechanism in HGCN.

 Table 10. Stress loss (\downarrow) when using embeddings from LP to predict pairwise shortest path graph distances with linear regression.

MODEL	DISEASE $\delta = 0$	AIRPORT $\delta = 2$	CORA $\delta = 4$	PUBMED $\delta = 4.5$	CITESEER $\delta = 6.5$
FEATURES	0.0842	0.0907	0.1507	0.0754	0.2584
MLP	0.0573 \pm 0.0003	0.0476 \pm 0.0005	0.1498 \pm 0.0000	0.0754 \pm 0.0000	0.2611 \pm 0.0004
GCN	0.0457 \pm 0.0011	0.0567 \pm 0.0009	0.1501 \pm 0.0001	0.0754 \pm 0.0000	0.2618 \pm 0.0004
GAT	0.0598 \pm 0.0007	0.0518 \pm 0.0012	0.1495 \pm 0.0001	0.0754 \pm 0.0000	0.2625 \pm 0.0007
HYBONET (EUCL.)	0.0506 \pm 0.0042	0.0661 \pm 0.0010	0.1563 \pm 0.0001	0.0754 \pm 0.0000	0.2618 \pm 0.0002
HYBONET	0.0316 \pm 0.0022	0.0396 \pm 0.0009	0.1561 \pm 0.0004	0.0754 \pm 0.0000	0.2652 \pm 0.0004
HGCN	0.0497 \pm 0.0032	0.0479 \pm 0.0027	0.1502 \pm 0.0021	0.0754 \pm 0.0000	0.2569 \pm 0.0006

Table 11. Stress loss (\downarrow) when using embeddings from LP to predict pairwise shortest path graph distances with linear regression. Values are normalized such that 1 corresponds to the same loss as with the distances computed directly in feature-space.

MODEL	DISEASE $\delta = 0$	AIRPORT $\delta = 2$	CORA $\delta = 4$	PUBMED $\delta = 4.5$	CITESEER $\delta = 6.5$
MLP	0.68 \pm 0.00	0.53 \pm 0.01	0.99 \pm 0.00	1.00 \pm 0.00	1.01 \pm 0.00
GCN	0.54 \pm 0.01	0.63 \pm 0.01	1.00 \pm 0.00	1.00 \pm 0.00	1.01 \pm 0.00
GAT	0.71 \pm 0.01	0.58 \pm 0.01	0.99 \pm 0.00	1.00 \pm 0.00	1.02 \pm 0.00
HYBONET (EUCL.)	0.60 \pm 0.05	0.74 \pm 0.01	1.04 \pm 0.00	1.00 \pm 0.00	1.01 \pm 0.00
HYBONET	0.38 \pm 0.03	0.44 \pm 0.01	1.03 \pm 0.00	1.00 \pm 0.00	1.03 \pm 0.00
HGCN	0.59 \pm 0.04	0.54 \pm 0.03	1.00 \pm 0.01	1.00 \pm 0.00	0.99 \pm 0.00

F.3. Node Regression

Here we provide additional results on the synthetic tree and grid datasets. Since for NR, we also train with a stress loss, but on the regression labels from the train set (instead of pair-wise shortest path graph distances), we report the results on the test set in Table 14. The findings remain the same as for MAE, HyboNet dominates on the tree dataset and the GCN/GAT on the grid. HGCN performs reasonably well on both datasets due to its learnable curvature. The curvature–performance trade-off for HGCN (with fixed curvature) shown in Figure 10 is also very similar as for the MAE. We additionally added the result for $d = 3$. Tables 13 and 14 provide a distortion analysis, measuring how faithfully the learned node representations preserve the input graph metric via the stress loss (Section 3). They show that no method does preserve pair-wise graph distances as measured by the Normalized Stress Loss on the tree and control dataset. This is expected since the task does not require the method to preserve the global geometry. In particular with the root node as anchor, models can completely ignore angular effects and collapse all node embeddings in the same level of the tree. On the grid dataset, GCN, GAT and HGCN do reduce distortion to some extend. By a similar analogy, using a central point as the center of the grid implies the grid geometry has to be preserved to some extent, particularly for smaller distances.

Table 12. Node Regression test stress loss (\downarrow) results on the synthetic tree and grid dataset for embedding dimension 3 and ≤ 128 .

MODEL	TREE		GRID		CONTROL TREE
	3	≤ 128	3	≤ 128	≤ 128
MLP	0.2144 \pm 0.0076	0.2236 \pm 0.0086	0.5772 \pm 0.1847	0.7364 \pm 0.3329	0.2319 \pm 0.0215
GCN	0.0375 \pm 0.0536	0.0341 \pm 0.0542	0.0029 \pm 0.0010	0.0027 \pm 0.0009	0.2229 \pm 0.0196
GAT	0.0708 \pm 0.0713	0.0104 \pm 0.0061	0.0053 \pm 0.0044	0.0022 \pm 0.0012	0.2184 \pm 0.0163
HYBONET	0.0044 \pm 0.0046	0.0008 \pm 0.0007	0.0583 \pm 0.0263	0.0069 \pm 0.0040	0.2198 \pm 0.0125
HGCN	0.0243 \pm 0.0072	0.0057 \pm 0.0020	0.0039 \pm 0.0022	0.0019 \pm 0.0014	0.2325 \pm 0.0217

Table 13. Normalized Stress Loss (\downarrow) on the synthetic tree and grid dataset using NR embeddings for dimension 3 and ≤ 128 .

MODEL	TREE			GRID	
	3	≤ 128	CONTROL	3	≤ 128
MLP	1.03 \pm 0.07	1.30 \pm 0.08	1.03 \pm 0.02	1.18 \pm 0.06	1.06 \pm 0.01
GCN	1.21 \pm 0.03	1.23 \pm 0.09	1.31 \pm 0.08	0.64 \pm 0.01	0.97 \pm 0.01
GAT	1.29 \pm 0.09	1.38 \pm 0.10	1.16 \pm 0.09	0.63 \pm 0.02	0.63 \pm 0.02
HYBONET	1.40 \pm 0.01	1.49 \pm 0.03	1.08 \pm 0.13	1.04 \pm 0.09	0.93 \pm 0.06
HGCN	1.25 \pm 0.15	1.23 \pm 0.23	0.90 \pm 0.03	0.83 \pm 0.11	0.86 \pm 0.15

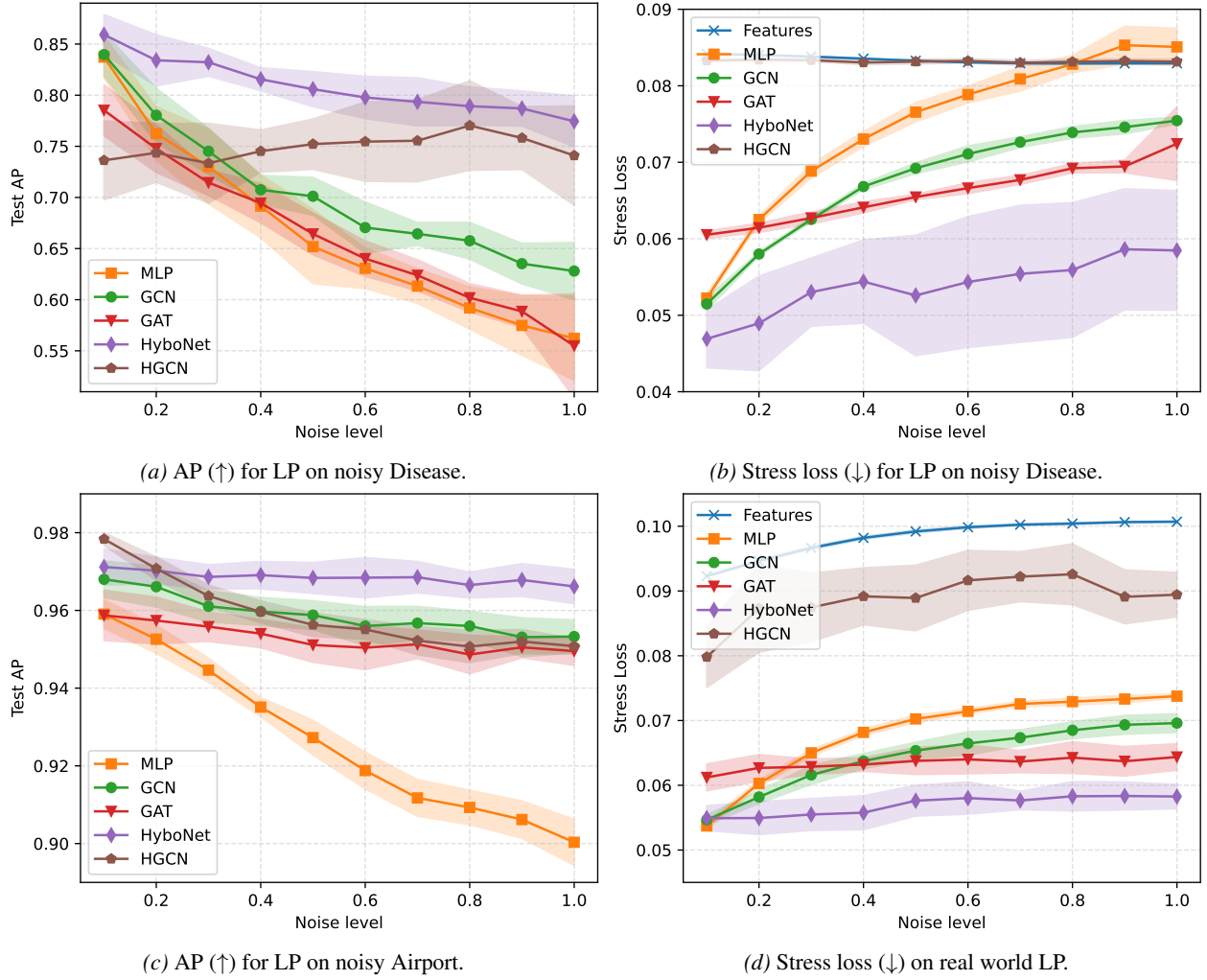


Figure 8. LP results (AP and Stress Loss) on real-world datasets Disease ($\delta = 0$) and Airport ($\delta = 2$) for different levels of noise added to the features. In all cases the GNNs clearly outperform the MLP and the hyperbolic methods on Disease and HyboNet on Airport outperform the Euclidean models.

F.4. Node Classification

Real-world datasets. As mentioned in the main text, in addition to the Macro F1 results, we also report accuracy (Acc) to give a more comprehensive picture. The full NC results on the real word datasets are in Table 15 for Macro F1 and Table 16 for Acc. As for the PDP task, we also include HyboNet (Eucl.) as an additional comparison to isolate the effect of model architecture here. The Acc results do not offer a completely new perspective on the model’s performance, but merely underline the findings already made for Macro F1. The reason for this is simply because most of these dataset are not very imbalanced, with the exception of Disease. If a model ignores the minority class, the accuracy results can still be good.

On the Disease* dataset with the 70/15/15% split that keeps the ratio of the two classes in all splits, we can see a larger difference between the Macro F1 and Accuracy columns in the two tables (Table 15 and Table 16). All models (with the exception of the MLP) achieve almost equally good performance w.r.t. to accuracy but using Macro F1, the differences become more pronounced. This is not the case for the old Disease results using the 70/5/25% split, with balanced 50/50% ratio in validation and test set, where naturally the F1 and the Accuracy results match more closely. We would also like to note, that the performance advantage of HyboNet is much more pronounced in this setting. This likely arises due to the very few training samples of the minority class in train set (due to the old splitting technique). In this case, the performance comes

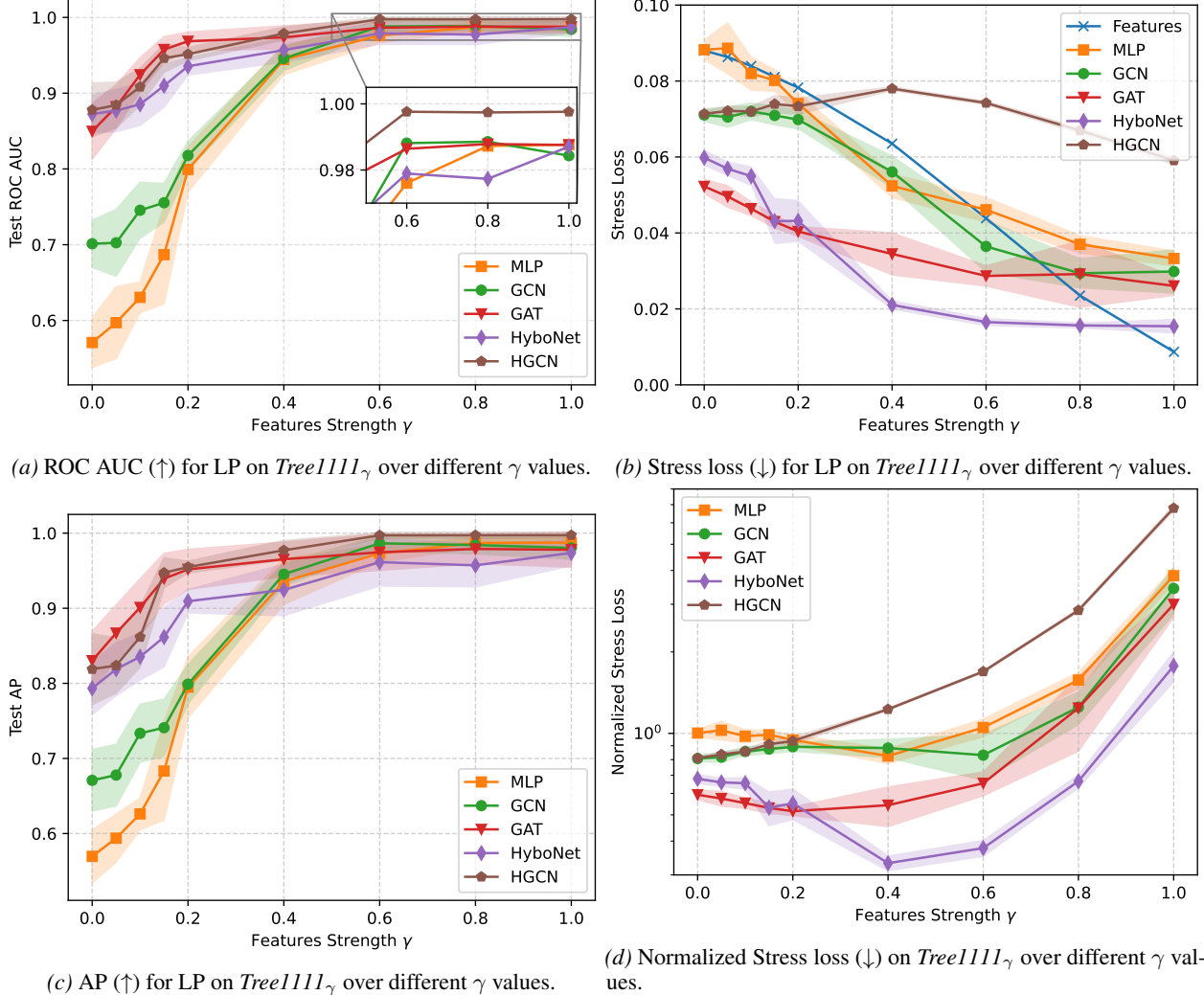


Figure 9. LP ROC AUC, AP, Stress Loss and Normalized Stress Loss on the synthetic Tree1111_γ datasets. γ encodes the features informativeness. The GNNs outperform MLP for small γ and GAT, HGCN and HyboNet perform best, while HyboNet achieves the smallest distortion as measured by the stress loss.

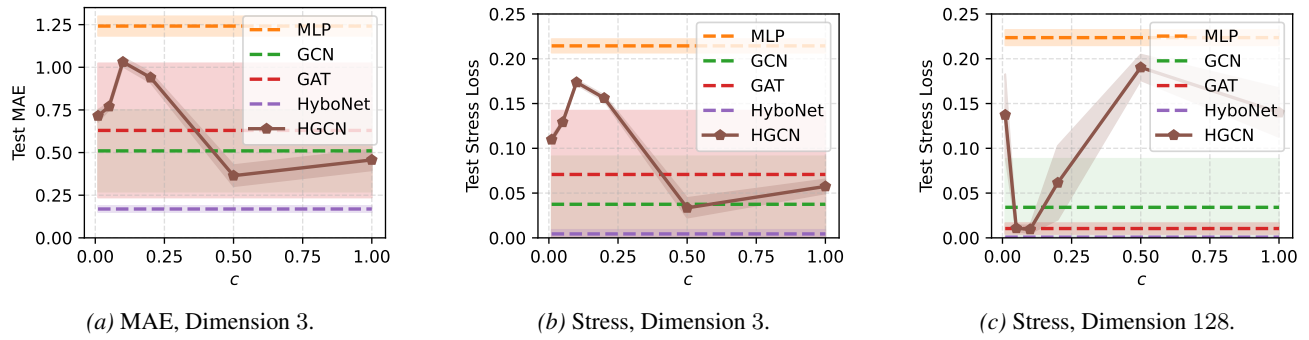


Figure 10. NR performance of HGCN vs. its fixed curvature magnitude c on the synthetic tree dataset. We report NR MAE (\downarrow) for hidden dimension 3 (a) and test stress loss (\downarrow) for hidden dimension 3 (b) and 128 (c).

more from the inductive bias in a heavily restricted sample regime (low sample complexity, which is something we proposed as future work), rather than from geometry of the task. For precisely this reason, we unified the splitting (sufficiently large

Table 14. Absolute Stress Loss (\downarrow) on the synthetic tree and grid dataset using the embeddings of dimensions 3 and ≤ 128 from Node Regression.

MODEL	TREE		GRID		CONTROL TREE
	3	≤ 128	3	≤ 128	≤ 128
FEATURES	0.1192	0.1192	0.5791	0.5791	0.1192
MLP	0.1226 ± 0.0085	0.1550 ± 0.0100	0.6860 ± 0.0368	0.6121 ± 0.0074	0.1231 ± 0.0030
GCN	0.1439 ± 0.0030	0.1467 ± 0.0105	0.3731 ± 0.0075	0.5625 ± 0.0077	0.1560 ± 0.0096
GAT	0.1539 ± 0.0104	0.1641 ± 0.0121	0.3637 ± 0.0087	0.3667 ± 0.0093	0.1380 ± 0.0105
HYBONET	0.1665 ± 0.0006	0.1775 ± 0.0039	0.6049 ± 0.0534	0.5409 ± 0.0355	0.1291 ± 0.0155
HGCN	0.1486 ± 0.0181	0.1463 ± 0.0270	0.4800 ± 0.0638	0.5007 ± 0.0873	0.1077 ± 0.0038

Table 15. Macro F1 scores (\uparrow) for real-world node classification (NC). We report Gromov δ -hyperbolicity (lower is more hyperbolic).

MODEL	DISEASE	DISEASE*	AIRPORT	CORA	PUBMED	CITESEER
	$\delta = 0$	$\delta = 0$	$\delta = 2$	$\delta = 4$	$\delta = 4.5$	$\delta = 6.5$
MLP	77.12 ± 7.53	48.62 ± 5.06	88.79 ± 1.97	55.63 ± 1.50	70.45 ± 1.12	54.29 ± 1.14
GCN	89.14 ± 2.33	89.50 ± 4.82	92.46 ± 0.86	80.09 ± 1.01	78.49 ± 1.47	64.95 ± 1.50
GAT	86.78 ± 9.14	85.71 ± 5.50	88.33 ± 5.73	80.71 ± 1.22	78.44 ± 1.88	65.16 ± 1.48
HYBONET (EUCL.)	89.18 ± 1.56	90.51 ± 3.74	90.54 ± 1.40	78.65 ± 1.04	78.55 ± 1.28	62.51 ± 1.67
HYBONET	94.42 ± 1.70	90.48 ± 5.12	90.87 ± 1.10	78.72 ± 1.01	78.33 ± 1.97	62.98 ± 1.48
HGCN	89.52 ± 1.60	90.51 ± 3.45	90.92 ± 2.04	78.34 ± 0.95	78.21 ± 1.47	63.29 ± 2.07

data to learn in all cases), resulting in a much more fair scenario to isolate the effect of geometry–task alignment.

Again, as for LP, for full disclosure, we report the exact values of Stress Loss for the distortion analysis for NC. The absolute values are in Table 17 and the normalized values are in Table 18. No model is able to significantly reduce distortion for any dataset.

Synthetic Datasets. We evaluate all our models on the synthetic tree graph we used in our NR experiments, the results are summarized in Table 19. Different from NR, we could not verify the performance advantage of HGNNs in this setting. In the embedding dimension ≤ 128 setting, GCN, HyboNet and HGCN are all able to perform perfect classification. Again they do this without preserving the graph structure as indicated by the (Normalized) Stress Loss. If we constrain the embedding dimension to $d = 3$, the results seem to indicate some advantage of hyperbolic methods, but with a few caveats. The results suggest that HGCN clearly performs best, with HyboNet following, but checking the standard deviations, GCN could also be among the best. The reason for this is that across the 10 splits, all models (except for HGCN and MLP), perform quite well, while on others they basically fail to learn the task. Now the hyperparameters were chosen only across 2 runs, on which all models (except MLP) performed quite well. All in all, the results suggest that in future work a more in-depth analysis is necessary to make a clear statement, maybe also considering sample complexity.

Table 16. Accuracy (\uparrow) results for node classification (NC) tasks. We report Gromov δ -hyperbolicity (lower is more hyperbolic). Note that accuracy on Disease is less meaningful in comparison to the other models than the one of Disease* due to class imbalance effects.

MODEL	DISEASE	DISEASE*	AIRPORT	CORA	PUBMED	CITESEER
	$\delta = 0$	$\delta = 0$	$\delta = 2$	$\delta = 4$	$\delta = 4.5$	$\delta = 6.5$
MLP	71.04 \pm 4.30	60.45 \pm 3.14	89.48 \pm 2.70	57.40 \pm 1.73	71.03 \pm 1.14	56.86 \pm 1.02
GCN	89.88 \pm 3.04	95.41 \pm 2.36	93.18 \pm 0.98	81.08 \pm 0.76	78.33 \pm 1.24	68.45 \pm 1.40
GAT	87.69 \pm 8.41	94.01 \pm 2.28	89.77 \pm 4.63	81.86 \pm 1.13	77.95 \pm 1.79	68.56 \pm 1.22
HYBONET (EUCL.)	89.46 \pm 1.99	96.11 \pm 1.46	91.51 \pm 1.35	79.84 \pm 1.06	78.04 \pm 1.13	66.35 \pm 1.30
HYBONET	94.50 \pm 1.85	95.99 \pm 2.23	92.05 \pm 1.54	79.89 \pm 1.14	77.91 \pm 1.81	66.76 \pm 1.95
HGCN	89.92 \pm 1.28	96.18 \pm 1.40	91.69 \pm 1.73	79.48 \pm 0.66	78.51 \pm 1.61	66.94 \pm 1.70

Table 17. Absolute Stress Loss (\downarrow) results of the real-world datasets when using embeddings from NC.

MODEL	DISEASE	DISEASE*	AIRPORT	CORA	PUBMED	CITESEER
	$\delta = 0$	$\delta = 0$	$\delta = 2$	$\delta = 4$	$\delta = 4.5$	$\delta = 6.5$
FEATURES	0.2301	0.2301	0.0907	0.1508	0.0754	0.2584
MLP	0.4700 \pm 0.1301	0.4249 \pm 0.1156	0.0833 \pm 0.0013	0.2820 \pm 0.0077	0.0754 \pm 0.0000	0.2572 \pm 0.0005
GCN	0.3098 \pm 0.0298	0.3465 \pm 0.0353	0.0930 \pm 0.0016	0.1495 \pm 0.0001	0.0754 \pm 0.0000	0.2652 \pm 0.0007
GAT	0.3057 \pm 0.0829	0.3447 \pm 0.0677	0.0832 \pm 0.0101	0.1503 \pm 0.0004	0.0754 \pm 0.0000	0.2698 \pm 0.0009
HYBONET (EUCL.)	0.2858 \pm 0.0270	0.3216 \pm 0.0184	0.0937 \pm 0.0011	0.1563 \pm 0.0001	0.0754 \pm 0.0000	0.2701 \pm 0.0007
HYBONET	0.2778 \pm 0.0270	0.2457 \pm 0.0219	0.0644 \pm 0.0042	0.1511 \pm 0.0001	0.0754 \pm 0.0000	0.2653 \pm 0.0011
HGCN	0.2861 \pm 0.0245	0.2627 \pm 0.0324	0.0834 \pm 0.0019	0.1512 \pm 0.0027	0.0754 \pm 0.0000	0.2578 \pm 0.0045

Table 18. Normalized Stress Loss (\downarrow) results of the real-world datasets when using embeddings from NC. Values are normalized such that 1 corresponds to the same loss as with the distances using directly the features.

MODEL	DISEASE	DISEASE*	AIRPORT	CORA	PUBMED	CITESEER
	$\delta = 0$	$\delta = 0$	$\delta = 2$	$\delta = 4$	$\delta = 4.5$	$\delta = 6.5$
MLP	2.04 \pm 0.57	1.85 \pm 0.50	0.93 \pm 0.01	1.87 \pm 0.05	1.00 \pm 0.00	0.99 \pm 0.00
GCN	1.35 \pm 0.13	1.51 \pm 0.15	1.04 \pm 0.02	0.99 \pm 0.00	1.00 \pm 0.00	1.03 \pm 0.00
GAT	1.33 \pm 0.36	1.50 \pm 0.29	0.93 \pm 0.11	1.00 \pm 0.00	1.00 \pm 0.00	1.04 \pm 0.00
HYBONET (EUCL.)	1.24 \pm 0.12	1.40 \pm 0.08	1.05 \pm 0.01	1.04 \pm 0.00	1.00 \pm 0.00	1.05 \pm 0.00
HYBONET	1.21 \pm 0.12	1.07 \pm 0.10	0.72 \pm 0.05	1.00 \pm 0.00	1.00 \pm 0.00	1.03 \pm 0.00
HGCN	1.24 \pm 0.11	1.14 \pm 0.14	0.93 \pm 0.02	1.00 \pm 0.02	1.00 \pm 0.00	1.00 \pm 0.02

Table 19. Macro F1 scores and Accuracy (\uparrow) and (Normalized) Stress Loss (\downarrow) for node classification (NC) on the synthetic tree dataset also used for node regression. The features loss for the normalization is 0.1192.

MODEL	MACRO F1		ACCURACY		STRESS LOSS		NORM. STRESS LOSS	
	3	≤ 128	3	≤ 128	3	≤ 128	3	≤ 128
MLP	22.69 \pm 2.27	21.80 \pm 1.79	35.15 \pm 9.53	35.24 \pm 8.70	0.1341 \pm 0.0088	0.3490 \pm 0.3242	1.13 \pm 0.07	2.93 \pm 2.72
GCN	70.62 \pm 29.87	100.00 \pm 0.00	75.75 \pm 26.36	100.00 \pm 0.00	0.1447 \pm 0.0108	0.1489 \pm 0.0044	1.21 \pm 0.09	1.25 \pm 0.04
GAT	69.09 \pm 18.16	69.96 \pm 12.10	69.09 \pm 18.16	63.36 \pm 14.49	0.1433 \pm 0.0438	0.1352 \pm 0.0098	1.20 \pm 0.37	1.13 \pm 0.08
HYBONET	79.78 \pm 31.81	97.99 \pm 3.21	82.78 \pm 27.13	98.85 \pm 2.10	0.1265 \pm 0.0131	0.1134 \pm 0.0228	1.06 \pm 0.11	0.95 \pm 0.19
HGCN	97.02 \pm 1.73	100.00 \pm 0.00	99.42 \pm 1.73	100.00 \pm 0.00	0.1457 \pm 0.0125	0.1304 \pm 0.0059	1.22 \pm 0.11	1.09 \pm 0.05